Published in final edited form as:
Adv Drug Deliv Rev. 2017 April ; 113: 61–86. doi:10.1016/j.addr.2016.05.023.

Imaging the pharmacology of nanomaterials by intravital microscopy: towards understanding their biological behavior

Miles A. Miller[1] and **Ralph Weissleder**[1,2]

[1]Center for Systems Biology, Massachusetts General Hospital, 185 Cambridge St, CPZN 5206, Boston, MA 02114

[2]Department of Systems Biology, Harvard Medical School, 200 Longwood Ave, Boston, MA 02115

Abstract

Therapeutic nanoparticles (NPs) can deliver cytotoxic chemotherapeutics and other drugs more safely and efficiently to patients; furthermore, selective delivery to target tissues can theoretically be accomplished actively through coating NPs with molecular ligands, and passively through exploiting physiological “enhanced permeability and retention” features. However, clinical trial results have been mixed in showing improved efficacy with drug nano-encapsulation, largely due to heterogeneous NP accumulation at target sites across patients. Thus, a clear need exists to better understand why many NP strategies fail *in vivo* and not result in significantly improved tumor uptake or therapeutic response. Multicolor *in vivo* confocal fluorescence imaging (intravital microscopy; IVM) enables integrated pharmacokinetic and pharmacodynamic (PK/PD) measurement at the single-cell level, and has helped answer key questions regarding the biological mechanisms of *in vivo* NP behavior. This review summarizes progress to date and also describes useful technical strategies for successful IVM experimentation.

Graphical abstract

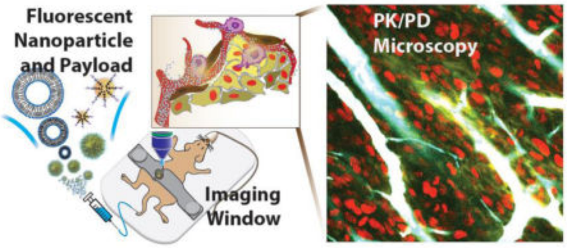

---

*R. Weissleder, MD, PhD, Center for Systems Biology, Massachusetts General Hospital, 185 Cambridge St, CPZN 5206, Boston, MA, 02114, 617-726-8226, rweissleder@mgh.harvard.edu.

Keywords

tumor associated macrophage; phagocyte; extravasation; microvascular perfusion; orthotopic window; drug efflux; liposome; polymer micelle; quantum dot; fluorophore

1. Introduction

A large number of nanoparticles (NPs) have been developed to deliver therapeutic compounds more safely and effectively to solid cancers and other target tissues [1–3]. Non-encapsulated cytotoxic compounds (e.g. doxorubicin, daunorubicin, taxanes, eribulin, epothilones, maytansines, camptothecins, platinum, irinotecan) along with some anesthetics (e.g., morphine), anti-fungals (e.g., amphotericin B), anti-helminths, antibiotics, and photosensitizers (e.g., verteporfin, used to treat macular degeneration) are often plagued by poor pharmacokinetic (PK) properties, and several of these must be intravenously administered over a prolonged periods because of side effects. A large body of work has demonstrated the possibility, and in some cases clinical success, of using NPs to encapsulate these drugs and pro-drug formulations, thereby eliminating the need for harmful solvents, extending the circulating half-life, and enabling controlled drug release [4–8]. Clinically approved NPs demonstrating such properties include liposomal formulations of doxorubicin (DOXIL, Caelyx, Myocet), irinotecan (Onivyde), amphotericin B (AmBisome, Fungisome), verteporfin (Visudyne), morphine (DepoDur), bupivacaine (Exparel), along with the nanoparticle albumin-bound paclitaxel (nab-paclitaxel, Abraxane), and many more NPs have progressed to clinical trials [8,9]. Despite this achievement and a demonstrated ability of NPs to reduce side-effects [6,10], the results of some clinical trials have been difficult to predict, particularly with regards to efficacy [11]. Furthermore, selective delivery of NPs to tumor cells has not substantially improved in the last 10 years by some measures [12]. These shortcomings largely arise from our limited understanding of *in vivo* NP transport and activity, along with an inability to predictably and robustly engineer such behavior, and thus highlight the need for better tools and perspectives into how NPs actually behave *in vivo.*

Particularly in cancer application, extensive studies have demonstrated nano-encapsulation can effectively i) facilitate precisely engineered combination therapies through co-encapsulation with additional drugs [13–16]; ii) enable the administration of more lipophilic compounds [17] and iii) modify tissue distribution and enhance intratumoral accumulation [7,12,18]. The latter is thought to occur through enhanced permeability and retention (EPR) effects that arise from interrelated physiological factors including abnormal and leaky vasculature at sites of inflammation and tumor growth; dysfunctional lymphatics and fluid drainage; unbalanced interstitial pressures from cancer and stromal cells impacting extracellular matrix (ECM); and mononuclear phagocytic system (MPS) activity within the tumor and inflammation sites, including from tumor associated macrophage (TAM). Collectively, the EPR effects contribute to what has been termed “passive NP targeting” [19]. In theory, enhanced permeability of the abnormal tumor vasculature or at a site of inflammation should allow NPs to enter the interstitial space, while suppressed lymphatic filtration and increased cellular uptake should allow them to stay there [18]. For many therapeutic NPs undergoing clinical trials in oncology [8,20,21], mixed results have presumably arisen from heterogeneous EPR effects combined with limited experimental data from patients on the effectiveness of EPR-mediated drug accumulation [22]. Furthermore, the inter-related *in vivo* pharmacokinetics and pharmacodynamics (PK/PD) of therapeutic NPs are more difficult to understand than those of the unencapsulated drug. NP drug delivery is inherently a multi-step process, defined by PK of the NP vehicle, drug release dynamics that may change depending on the *in vivo* environmental context, and PK of the cytotoxic payload itself. Little experimental evidence describes how this multi-step drug delivery sequence performs *in vivo* and within tumors despite its critical importance to overall therapeutic outcome. This lack of understanding clearly represents a bottleneck in the design and development of more efficacious therapies.

The active targeting of NPs to specific cell populations (including tumor cells) via affinity ligands on the NP surface has been proposed for directing specific NP retention and cellular uptake. Ligands are typically selected to bind surface molecules or receptors over-expressed in diseased organs, tissues, cells or subcellular domains [1]. Examples include prostate specific membrane antigen (PSMA) [3], somatostatin receptor (SSTR) [23,24] or folate receptor (FR) among others [1,25]. While early animals studies often show convincing differences in tumor accumulation between targeted and non-targeted preparations (or target expressing tumors vs non-expressers), on average the benefit of targeting is highly heterogeneous [12], highly dependent on the tumor model and tissue type [26], and clinical results are often not strongly convincing [8,27–29]. This begs the questions of whether the more limited clinical efficacy is due to different human PK, human heterogeneity poorly modeled in mice, different target expression levels in humans, or different human entry criteria into trials.

Compared to the vast literature on the synthesis of new nano-preparations and the common conceptual frameworks applied to how they might work (mostly derived from older biophysics measurements often on liposome and proteins), detailed analyses of how these materials actually work *in vivo* at the single cell level has traditionally been much more scant and largely confined to the last few years [30–53]. This is not entirely surprising as the technology to obtain this single cell data data has only recently matured and now allows high resolution imaging in orthotopic environments [54–56].

Our lab has invested considerable effort in developing *in vivo* imaging approaches at single-cell resolution necessary to resolve heterogeneous cell populations (intravital microscopy; IVM), with application to the integrated pharmacokinetic (PK) and pharmacodynamic (PD) properties of therapeutic NPs (Figs. 1, 2). The advantages of IVM over other approaches are summarized in Box 1 and essentially entail the ability to resolve cellular detail over time in live systems. As such, IVM is not a high throughput method (that is, large cohorts of mice are often infeasible) but rather a high-content method (that is, IVM produces detailed multiplexed measurements of physiology, pharmacology and biology). By imaging the localization of drugs, NPs, and ensuing cellular effects, IVM has helped demonstrate i) that nanotherapeutics can actively co-opt host phagocytes — primarily TAM — for drug delivery [39,43,55], ii) that clinical TAM imaging can stratify tumors for predicting therapeutic NP accumulation and longitudinal response to nano-encapsulated taxanes [54], iii) that TAM depletion can reduce both intratumoral accumulation and efficacy of the therapeutic NPs

[55], and iv) how taxane transport and efflux governs efficacy in vivo [56–58], all of which have important implications for further NP design and for selecting patients into NP trials. Beyond these initial observations - summarized below - the technology is ready to be applied to other pharmaceutical nano-preparations, other disease applications and different model systems. Box 2 summarizes some of the current questions for which IVM is particularly suited to obtain answers.

Box 1

Advantages of IVM over other analytical methods

1. Allows temporal analysis over hours - days
2. Allows spatial resolution often not detectable by whole body imaging techniques
3. Allows analysis of cellular heterogeneity
4. Allows mapping of cellular PK and PD across populations of cells
5. Yields mechanistic insight into NP drug actions
6. Through multichannel imaging, allows simultaneous analysis of different compounds, cells or biological processes
7. Allows rapid and unequivocal evidence whether newly designed nanoformulations work in vivo
8. Each mouse serves as it’s own control; allows reduction of large cohorts of animals
9. Compatible with expanding array of genetically engineered mice, cells and humanized models
10. Allows concomitant analysis of host response in addition to tumor

Box 2

Critical questions in nanomedicine that can be addressed by IVM

1. What are the physiological and mechanistic barriers to therapeutic NP accumulation in target cells?
2. What determines cellular patterns of NP uptake and distribution?
3. Do “tumor targeted” therapeutic NPs (both NP vehicles and their payload) reach their intended target (cancer cells) or do they accumulate in host cells (and if yes in which types)?
4. How much does molecular targeting with affinity ligands help in terms of NP distribution and effectiveness?
5. Can NP targeting and efficacy be optimized by other (e.g., adjuvant) strategies?

6. What is the cellular correlation between local drug concentrations and anti-tumor effects?
7. Are there bystander effects that explain the local anticancer effects of some nanotherapeutics such as taxanes [Mitchison, 2012, Mol Biol Cell, 23, 1–6]?
8. What biological mechanisms govern NP clearance and toxicity?

The intent of this review is to summarize i) the technical advances in the field of intravital imaging as they apply to nanotechnology drug testing, ii) our knowledge of NP distribution (PK) in mouse models and iii) how PD measurements can be made and be translated into clinical trials. In as second section we provide some of the technical aspects on nanoparticle labeling (Figs. 3, 4).

2. Discovering NP action by high resolution IVM imaging

2.1. How do nanoparticles selectively gain access to target cells?

Generally the most apparent and clinically evident advantages of drug nano-encapsulation arise from its ability to eliminate the need for harmful solvents, extend drug half-life in circulation (Fig. 5), and enable reduced dosing and peak drug concentrations that cause systemic toxicity [4–6]. At the same time, extended systemic drug exposure and serum half-life correlate with improved exposure profiles in target sites such as the tumor [59,60], and this observation generally applies not just to NPs, but to small molecule payloads, antibodies [61] and other biologics [62] as well. Although systemic PK and clearance can have profound impacts on drug safety and efficacy, the vast majority of NP-based drug delivery research has focused at the target site of drug action itself, asking the key question: how can selective NP uptake and drug release at the target site be maximized? This question is typically addressed by exploiting a variety of strategies, from enhanced permeability and retention (EPR) effects, to molecular or cellular targeting, to environmentally responsive drug release.

2.1.1. Microvasculature and permeability at target sites—IVM has become a standard tool for assessing changes in vascular structure and neovascularization at drug target sites, and especially as a response to therapeutic intervention, for example in response to anti-angiogenesis treatments such as anti-vascular endothelial growth factor receptor (α-VEGFR) antibody therapy [63]. In the context of NPs, IVM has helped parse the competing positive and negative influences of α-VEGFR treatment on NP transport. While α-VEGFR2 treatment normalizes vascular structure and allows for greater tumor perfusion by NPs, the treatment also reduces vessel permeability and therefore restricts tumor penetration, especially for larger NPs [34]. However, for NPs 40 nm and smaller, the former effect dominates and anti-angiogenic therapy improves NP delivery [34]. Other IVM studies support these general conclusions, showing that small NPs can diffuse into even poorly permeable tumors such as often found with pancreatic cancer, but that larger nanoparticles (50 nm diameter and greater) can become substantially limited in these cases [50]. In poorly permeable tumors, treatments with transforming growth factor β (TGFβ) increase permeability and improve penetration of larger NPs [50]. Nevertheless, when tumor vasculature is highly permeable, both small and large NPs readily accumulate even without adjuvants like TGFβ [50]. NP differences in tumor penetration are most pronounced at the microscopic single-cell level, as measured by IVM [50,54]; in contrast, correlation in macroscopic tumor uptake between NPs of contrasting size (~20 nm vs. ~100 nm) and coating (dextran vs. PEG) can still be strong [54]. Similarly, another study used IVM to examine differences in tumor uptake between filamentous and spherical PEGylated virus NPs, and found nearly identical uptake averaged across the entire tumor, but substantial differences in penetration at microscopic (~100 μm) length scales, particularly in the tumor core [49]. Precisely synthesized PRINT (Particle Replication in Non-Wetting Templates) NPs have been used to tightly control NP dimensions and minimize polydispersity, and one recent report investigated the distribution of distinctly shaped (55×70 nm compared to 80×320 nm) NPs within tumors. As expected, the smaller NPs were taken up by a somewhat greater fraction of macrophage and cancer cells, which suggested greater NP penetration. Yet surprisingly, the NP shape had little impact on uptake in other cell types such as the endothelium, and little effect on how much NP was taken up overall [31]. These results collectively suggest that primary EPR effects, particularly those related to microvascular structure, convection, perfusion, and phagocyte infiltration, may broadly apply to multiple NP types [54], whereas local NP extravasation, free diffusion, and penetration into tissue is much more size and shape dependent [34,50]. Future high-resolution imaging may eventually allow for greater mechanistic understanding of transport processes, particularly extravasation and the role of movement through intercellular gaps, transendothelial cell pores, and transcytosis [12].

Dynamic permeability and perfusion: With respect to vessel permeability, recent studies have elucidated how NP [30] and macromolecular [64] extravasation is a highly dynamic process characterized by transient bursts of NP tissue penetration, with significant contribution from perivascular macrophages that extend cellular processes through the endothelium [64] and that can even rapidly accumulate NP [54] within minutes. Furthermore, recent studies have shown that staggering the injection of differently colored, but otherwise identical, NPs by two hours leads to disparate penetration into tumor tissue at the microscopic scale, which underscores how burst-release patterns and even vascular perfusion change over time [33]. Overall, IVM has revealed that microvasculature structures and the process of NP transport from vessels into tissues is highly complex and dynamic at the microscopic length scale. To better understand such complex transport processes, *in vivo* imaging datasets have been useful for quantitative modeling and kinetic parameter estimation, which in turn describes differences between NPs and key limiting factors in their transport [30,54,65].

2.2. Are tumor targeted NPs better than EPR-mediated NPs for tumoral delivery?

Active molecular targeting of NPs to certain cellular populations, including tumor cells, immune cells, and endothelial cells, has been extensively developed for both therapeutic and diagnostic applications [1]. For targeted NPs, generally the first PD reaction consists of the NP's molecular targeting ligand binding to its receptor, which in drug delivery applications includes prostate-specific membrane antigen (PSMA); folate receptor (FR); epidermal growth factor receptor (EGFR) and the closely related HER2; the α_v,β_3 integrin; epithelial cell adhesion molecule (EpCAM); the blood platelet gC1qR; the mannose receptor expressed on macrophage; ECM components collagen IV and fibronectin; the transferrin receptor and others [1]. Strategies to target NPs are diverse, with targeting ligands that range from small molecules to sugars, polypeptides, protein fragments, nucleic-acid aptamers, full proteins and antibodies. Selective binding *in vivo* is highly complex and depends not just on ligand specificity and binding kinetics (k_{on}/k_{off}), but on ligand density, orientation, charge, hydrophobicity, size, and shape on the NP. PK, plasma-protein binding, opsonization, degradation, and aggregation also impact the binding ability. Thus, effective target binding is a multifactorial product of various *in vivo* physicochemical factors, and IVM addresses this complexity by allowing direct *in situ* visualization. Unfortunately, although early preclinical studies often show the beneficial impact of NP-targeting, results in orthotopic animal models, particularly in metastatic breast cancer [26] and in the clinic [28] are frequently less convincing. In a recent meta-analysis of over 100 studies, active targeting increased tumoral NP uptake by an average of 50% (from 0.6 to 0.9 % injected dose), but with extreme heterogeneity such that >25% of all passively targeted NPs performed better than >50% of all actively targeted NPs [12]. This raises questions of which mechanisms actually govern NP targeting efficacy *in vivo,* how these depend on tissue-type, and how mouse model results translate to the clinic and human pathophysiology.

2.2.1 Passive versus active NP targeting—IVM promises to be an important tool for parsing the impact of molecular NP targeting on otherwise passive EPR-driven accumulation, and several studies have already highlighted its potential. Molecularly-targeted agents, most prominently antibodies, are known to be susceptible to the “binding site barrier” effect, whereby successful binding to tissue near vasculature actually blocks penetration deeper into tissue [66]. To some extent, similar observations have been made with targeted NPs. For instance, *in vivo* imaging of PEGylated folate in tumors that overexpress folate-receptor has revealed poor tissue penetration compared to non-PEGylated folate-rhodamine. Perivascular tissue uptake and apparent PEG-folate endocytosis could be blocked by saturating the folate receptor with a folic acid derivative, which thus demonstrated the dependency of NP accumulation on target binding [25]. One study recently examined the trade-off between PK and receptor-binding PD using NPs that targeted tumor tissue via hyaluronic acid (HA) [67]. In this instance, NP PEGylation was found to adversely decrease the binding affinity of HA-NP to tumor cells *in vitro;* however, *in vivo,* the greatly extended plasma half-life, decreased liver clearance, and presumably enhanced EPR effects actually led to more tumoral accumulation with the PEGylated HA-NP, which was visualized by IVM and quantified by whole-organ imaging *ex vivo* [67].

For some applications, NPs are targeted to the vasculature itself. For instance, the peptide Arg-Gly-Asp (RGD) is frequently used to target neo-vasculature via $\alpha_v\beta_3$ integrin binding, and IVM allows for high-resolution measurement of NP binding and retention on the capillary walls of a tumor [68] and inflamed skin in a model of adjuvant-induced arthritis [69]. Imaging of RGD-functionalized quantum dots (Qdots), which bind $\alpha_v\beta_3$ integrin on inflamed or newly formed vasculature, has shown that NPs indeed bind to tumor vasculature with 2.5–10 fold selectivity over matched healthy vasculature, depending on the dose and tumor model [52,70], while the low-affinity peptide variant RAD does not. Interestingly, these [52,68,70] and older studies with doxorubicin-encapsulated RGD-liposomes [71] show uneven RGD-NP binding and uptake on microvasculature, possibly related to heterogeneous integrin availability, variable fluid dynamics, or a potential favorability towards multivalent binding with aggregates of large surface area.

Examination of RGD-targeted NPs has elucidated the importance of binding and receptor dynamics in governing the balance between EPR and active targeting. In one study, tumoral accumulation of RGD-functionalized single-walled carbon nanotubes (SWNT) was compared by IVM with the low affinity RAD-functionalized control. Perhaps unsurprisingly, the targeted NP exhibited greater tumor accumulation at early time points within six hours of administration, while passive tumor penetration and EPR effects dominated accumulation at later time points. Unexpectedly however, NP targeting again led to enhanced tumor retention at very late time points (>1 week post-administration), while non-targeted NPs were no longer detectable [72]. These results are somewhat consistent with another study that found RGD-liposomes could transiently saturate binding sites on vasculature. Using a combination of time-lapse IVM, time-lapse DCE-MRI, and *in vitro* experiments with repeated NP dosing, researchers found that RGD-NPs rapidly bound target, then stalled in uptake due to receptor saturation, and then began accumulating again once the binding sites were recycled or re-synthesized [44].

2.2.2. Receptor-mediated intracellular NP transport—The above study highlights the importance of receptor-mediated endocytosis and recycling in governing the effectiveness of NP targeting. Receptor trafficking, cell-membrane dynamics, and resultant cell behavior can depend on local mechanical and environmental context [73], and IVM addresses this complexity by enabling direct visualization of intracellular NP transport within *in vivo* contexts themselves. In fact, measurements of intracellular NP trafficking reveal striking divergence between *in vitro* models and complex behavior *in vivo.* For instance, in a study of Qdots targeting cancer cells by binding protease-activated receptor 1 (PAR-1), IVM tracked the movement of NPs across the cell surface *in vivo.* These measurements enabled calculation of mean-square-displacement and effective diffusion coefficients for surface-bound Qdots at subcellular resolution, and reveal a startlingly dynamic membrane fluidity. As invading tumor cells extend pseudopodia during migration and intravasation, protruding membranes become increasingly fluid, and fluidity reaches a maximum once cells actually enter circulation [51]. Receptor endocytosis is also complex; at the simplest level, imaging shows that the model compounds dextran and transferrin both exhibit measurable differences in internalization kinetics *in vivo* compared to in cell culture [74]. IVM of HER2-targeted Qdots has revealed a more complete and dynamic model of NP binding and receptor trafficking: once targeted NPs have extravasated into the tumor tissue, they bind to surface receptor and traffic to perinuclear endocytic vesicles in a discrete stepwise fashion characterized by periods of relative immobility followed by spurts of directional transport [75]. Similar stepwise “diffuse-and-go” or “stop-and-go” intracellular vesicle movement has been observed *in vivo* for Qdots taken up by neutrophils in a model of inflammation [76]. Ultimately, understanding how receptor-mediated NP binding and uptake occurs *in vivo* has helped show key limitations to targeted-NP efficacy, and may help guide new strategies for more efficiently targeted NP strategies.

2.3. Is there a competition between tumor cells and TAM and what does it mean?

NPs are primarily cleared from the body through the MPS, which includes macrophages of the liver (Kupffer cells) and spleen. In most applications MPS clearance is intentionally minimized to extend serum half-life and allow NPs more time to reach their intended targets; such immune avoidance is typically accomplished via PEGylation [59], although new strategies such as self-peptide presentation have also reduced unwanted MPS clearance [60]. IVM has been useful in parsing the effect of macrophages and other phagocytes on NP clearance, for instance showing how systemic PK of NPs is influenced by mouse strain and corresponding propensities for Th1 vs. Th2 immunological responses [77]. Th2-prone mice clear NPs at a faster rate than Th1-proned strains, which is logical considering Th1 responses are typically associated with intracellular pathogens, while the Th2 response is associated with targeting extracellular pathogens including bacteria, parasites, and other naturally occurring NPs [77]. Imaging after pharmacological depletion of phagocyte populations furthermore shows that both granulocytes and macrophages profoundly impact systemic PK, and macrophage polarization from an inflammatory/M1 phenotype to a wound-healing/M2 phenotype corresponds with increased NP uptake [77]. In the same vein, tumor inoculation and progression in mouse models cause an increase in tumor-promoting M2 macrophages, which then causes increased NP clearance [78].

Despite a recognized role in NP clearance, macrophages and other phagocytes are increasingly being appreciated as actively migrating conduits for targeted NP delivery, and IVM studies have been critical for discovering these new roles (Fig. 6, Fig. 7). Furthermore, many solid tumors contain large populations of infiltrating macrophages and other phagocytes, which themselves are therapeutically targeted to convert their behavior from a tumor- and metastasis-promoting M2 phenotype to a tumor-killing M1 phenotype [79]. Thus for cancer and other diseases where phagocytes play important auxiliary roles, it is an open question as to whether NPs should co-opt or completely avoid phagocyte uptake.

2.3.1. Directly targeting phagocytes—It was long ago appreciated that NP affinity towards phagocytes could actually be exploited for drug delivery. Some of the earliest nano-formulation strategies were developed to directly target macrophages in the context of adjuvant immune stimulation [80,81] and in infections such as leishmaniasis, histoplasmosis, staphylococcus, and cryptococcosis [82,83]. New immunological applications in infectious disease, oncology, rheumatology, vaccine development, and basic science continue to be developed for NPs, and high-resolution IVM has contributed to improvements in both biological understanding and therapeutic strategy.

Intravascular phagocyte delivery: *In vivo* imaging offers insight into how NP uptake in phagocytes actually governs their behavior and ultimate drug response, for instance revealing new concepts of chemotactic cellular transport of NPs into target tissues by activated immune cells. In one recent study, high aspect-ratio SWNTs are rapidly taken up by monocytes in circulation, and these cells then extravasate into tumor tissue [43]. The surprising cellular-based dynamics of SWNT uptake while still in circulation represents a generalizable concept of active drug delivery and substantially complicates how systemic PK is interpreted. As a similar example, IVM was used to discover that a denatured-albumin based NP is taken up selectively in activated neutrophils at sites of inflammation. More specifically, neutrophils in post-capillary venules accumulate the NP before migrating into the inflamed tissue, thereby actively transporting NPs selectively from circulation into target inflammation sites [39]. In a zebrafish model of tuberculosis, *in vivo* imaging showed that nano-encapsulated antibiotics could be actively delivered to granulomas via initial accumulation in circulating macrophage, which then extravasate at sites of infection [84]. As another instance of NP uptake within phagocytes, simultaneous *in vitro* imaging of DiD-labeled liposomes and their endogenously fluorescent daunorubicin payload shows that bone-marrow engrafting leukemia cells accumulate substantial NP in endosomal/lysosomal vesicles, from which daunorubicin releases and accumulates in the nucleus [85]. Thus, NP uptake in circulating cell populations, including monocytes, tuberculosis-infected macrophages, but also leukemia cells and circulating tumor cells [86] from solid cancers, may comprise an important and general feature of plasma PK and an advantageous feature for selective NP delivery.

Extravascular phagocyte delivery: Once NPs reach their target by vascular perfusion and extravasation, their uptake and retention in cells often becomes the next step in delivery, and IVM has been a helpful technology for quantifying the kinetics of NP uptake and payload release at the single-cell level. Many NP vehicles are targeted to immune cells, and fluorescence imaging has been used to visualize uptake in phagocyte populations including circulating monocytes [43,72], TAM [55], M2-like tumor promoting macrophages [87], M1-like inflammatory macrophages [88], atherosclerotic-plaque associated macrophages [89], neutrophils [90], dendritic cells [91], and tuberculosis-infected macrophages [84]. Fluorescent genetic reporter mice enable single-cell imaging of NP uptake into defined host cell populations. For instance, monocyte-derived cells including macrophages, dendritic cells, and neutrophils have been imaged using c-fms$^{YFP/+}$and CX3CR1$^{GFP/+}$genetically engineered mouse models (GEMMs) [54,55,88], showing that phagocytes lining vessels in adipose [88] or tumor [54,55] tissue avidly accumulate NPs within minutes. For targeted latex NPs that have been coated with phosphatidylserine (PtDSer) and the oxidized cholesterol derivative cholesterol-9-carboxynonanoate, macrophage uptake is even faster in the M1-phenotype adipose macrophage of obese mice, compared to the M2-polarized macrophage in lean adipose tissue [88]. Changes in NP size, for instance as precisely manipulated using PRINT technology [31], likewise shift the relative propensities of NPs for different cell populations including neutrophils and macrophages [31]. Similar comparisons using IVM have shown that smaller dextran NPs are much more avidly taken up by phagocytes compared to larger PEGylated NPs, which accumulate in both tumor cells and phagocytes alike [54]. Collectively, these studies show that extravascular and especially perivascular phagocytes accumulate a substantial amount of NPs in target tissues; that physicochemical NP modifications can bias uptake to various phagocyte populations; and that the kinetics of cell uptake can vary enormously, ranging from minutes to days depending on the particle characteristics.

NP degradation and payload liberation: Even if NPs have accumulated at or near their target tissue or in associated phagocyte populations, the concordant biodistribution and bioavailability of their therapeutic payload still determines ultimate drug activity. To address this issue, the NP vehicle and its therapeutic payload can be simultaneously tracked using multicolor fluorescence microscopy. As one example, dual imaging of a polymeric NP vehicle and its therapeutic platinum payload shows that even though TAM accumulate substantial NP, the chemotherapeutic payload is still able to diffuse to and influence neighboring tumor cells within a ~25 μm radius [55]. However, such local redistribution of drug payload from one cell to another depends on properties of the nano-formulation. In contrast to the previous example, PEGylated liposomal doxorubicin (DOXIL) was found to largely sequester in lysosomes where it co-localizes with its DiD-labeled liposomal vehicle [48]. Detrimental doxorubicin sequestration can be improved by stimulating NP degradation and drug release, as demonstrated recently by using a thermosensitive liposome and inducing local hyperthermia [37,47]. In this case, multicolor IVM measured the combined PK of the NP vehicle and its payload. Hyperthermia causes rapid doxorubicin release from the vasculature out into the tumor tissue, leading to 1.7-fold enhanced drug accumulation in the tumor. Ultrasound has also been used to stimulate local tissue hyperthermia and increase vascular permeability, and imaging reveals the process to be very rapid. Within 3 minutes, local ultrasonication enhances the extravasatation of large nanodroplets (>200 nm) by 4.7 fold, and leads to a near emptying of smaller 20 nm polymer NPs from capillaries into the neighboring tumor tissue [36].

Although dual-color imaging of the NP vehicle and its payload allows for divergent PK and spatial distributions to be observed, this approach does not directly reveal how the structure and components of the NP itself change or degrade. As a solution, FRET-based methods reveal chemical or physical transformations of the NP by their influence on separating FRET-paired dyes or bringing them close together. For example, FRET between a NIR-emitting, PEGylated Qdot core and its Cy7-lipid coating was monitored by IVM and revealed a surprising and rapid decrease of FRET in circulation. In this case, lipids on the Qdot rapidly exchanged or transferred to plasma protein components in the blood. Also surprisingly, extravascular NPs degraded at a slower rate compared to those in circulation, likely reflecting the different abundances in plasma components and lipoproteins [92]. Similarly rapid dye exchange was observed using the lipid dye FRET pair DiD and DiR in poly(ethylene oxide)-b-polystyrene NPs, but the rate in FRET decrease could be slowed 5-fold by doping additional lipids into the nano-formulation [93]. Overall, IVM is a useful tool for visualizing stability, uptake, and re-distribution of NPs and their payload, which can determine whether phagocytes serve as a source or sink of drug delivery to neighboring target cell populations.

2.3.2. Cellular PD response reveals extent of TAM drug-depot effects—

In many cases, the mere spatial distribution and binding of a drug or NP to its target fails to influence downstream biological pathways and cellular behaviors in predictable manners. Consequently, it is generally necessary to monitor distal cellular and disease phenotypes after drug treatment, and this especially applies to complex *in vivo* environments where neighboring cells (including TAM) can cause indirect or bystander drug effects through cell-cell signaling events [94] and oxidative stress [95]. Multicolor imaging supports simultaneous correlation of cellular PD responses with PK on a cell-by-cell basis; provides a quantitative means of assessing dose-response PK/PD relationships; gauges how heterogeneous cell responses are to a given drug exposure; and determines how reliably a given PD response correlates with downstream phenotypic change. For instance, in one study the PK of a dual-labeled polymeric nanoparticle and its cytotoxic cisplatin-related prodrug were simultaneously monitored with tumor-cell PD responses. Single-cell DNA damage response was assessed by foci formation of a fluorescent DNA-damage response protein, which was also monitored over time for its co-segregation with DNA to indicate mitosis [55]. As expected, time-lapse IVM data showed highly heterogeneous drug exposure and cellular response driven by drug nano-encapsulation. Yet surprisingly, automated computational analysis was able to attribute much of the variability to host phagocytes including TAM, and a clear correlation was found between local phagocyte density and the amount of drug accumulation and DNA damage in neighboring tumor cells. From these data, further experiments were performed to confirm that TAM served as cellular depots for accumulating NPs and locally releasing their DNA-damaging payload [55]. As another example of dual PK/PD imaging, the delivery of a fluorescently-labeled nano-encapsulated inhibitor of P-glycoprotein (P-gp; also known as multidrug resistance protein 1, MDR1) was monitored simultaneously with its PD effect on chemotherapeutic efflux from individual tumor cells [56]. Similar to the example above, in this case tumoral NP delivery was very heterogeneous and localized primarily to tumor vasculature and neighboring tumor-associated phagocytes. However, in stark contrast to the cisplatin and DNA damage example, the MDR1 inhibitor homogeneously blocked MDR1 activity and drug efflux across the vast majority of tumor cells. This occurred despite heterogeneous uptake of the NP vehicle itself, presumably because the drug was efficiently liberated from its NP vehicle and broadly redistributed to the rest of the tumor [56]. These two studies underscore the importance of combined PK/PD imaging, demonstrate how mere emphasis on PK or upstream PD effects alone may yield an incomplete understanding, and exemplify how local NP delivery to TAM can lead to distinct spatially-dependent effects on neighboring tumor cells.

2.4 How can NPs overcome delivery barriers?

Drug resistance is an inevitable feature of many cancers and infectious diseases, and occurs through mechanisms related to PK and PD. PK-driven resistance occurs largely through upregulation of drug-transport proteins, especially P-gp/MDR1, and through physiological barriers to drug delivery, such as the development of fibrous tissue (desmoplasia), and nano-formulation is an important consideration in both instances.

2.4.1. Resistance through drug efflux and metabolism—IVM supports quantitative measurements of drug efflux within tumors at the single-cell level, as was recently demonstrated in a study of a fluorescently-labeled microtubule-targeting agent, eribulin mesylate [56]. Surprisingly, fluorescence imaging revealed that although eribulin has been clinically developed for treating taxane-resistant cancers, taxane treatment and subsequently emergent resistance likewise affects eribulin sensitivity as well, principally through shared mechanisms of drug efflux. Other resistance-inducing transport mechanisms have been similarly studied using fluorescent-drug conjugates, including those related to platinum such as the copper transporter pathway [96,97] and subcellular (for instance, mitochondrial) accumulation of platinum derivates [98]. NP delivery represents a promising strategy to overcome resistance related to intracellular drug transport and efflux. In the case of platinum therapies, NPs have been developed to selectively dissociate and deliver oxaliplatin-prodrug within late endosomes, which is thought to enhance delivery to the nearby nucleus where it forms cytotoxic DNA adducts [53]. IVM enabled visualization of fluorescent NP transport, and fluorescence de-quenching revealed selective NP disruption in perinuclear endosomal/ lysosomal compartments in the tumor [53]. In contrast, un-encapsulated oxaliplatin is more susceptible to cytoplasmic detoxification systems such as metallothionein and methionine synthase, and hence is less potent, especially in resistant tumor models [53]. With regards to eribulin and similar P-gp/MDR1 substrates (most notably doxorubicin), many MDR1 inhibitors have been developed to overcome drug resistance but with limited efficacy and with toxic increases in systemic drug exposure [99]. Nano-encapsulation of MDR1-inhibitors including tariquidar [100] and HM30181 [56] enhances the activity of MDR1-substrate chemotherapeutics such as doxorubicin [100], and has been imaged *in vivo* [56].

2.4.2 Stromal and mucosal barriers to efficacy—Outside of and surrounding target cell populations, stromal and mucosal barriers to drug penetration often contribute to drug resistance in infectious disease [101] and cancer [102]. Many nanoencapsulation strategies aim to improve penetration through physiological pulmonary, nasal, orogastric, intestinal [103], transdermal, and blood-brain barriers [104], along with pathological obstructions such as mucus [105], desmoplastic tissue [102], and microbial biofilm [106]. *In vitro* NP imaging and particle tracking has been useful for quantifying the effect of physicochemical NP properties, including charge and PEGylation, on effective transport through biofilm [106], cystic-fibrosis sputum [107], and ECM [108]. In cancer development, a confluence of stromal factors contribute to poor NP penetration, including NP ionization via acidic tumor microenvironment; electrostatic particle filtering by charged ECM components such as the negatively-charged heparin sulfate along with the positively charged perlecan complex and nidogen; ECM thickening, stiffening, and cross-linking; and increased interstitial fluid pressure via high density tumor-cell packing, dysfunctional vascular/lymphatic perfusion and fluid drainage, and fibrosis [102]. Fluorescence and multiphoton microscopy have enabled direct visualization of some of these features [109]. For instance, fibers of collagen (and particularly collagen IV) are key components of the basement membrane, which is a fibrous barrier to NP delivery that separates many neoplastic and healthy tissues from underlying stroma, and are readily visualized by second harmonic generation (SHG) multiphoton microscopy. Recent *ex vivo* studies have found correlation between NP permeability and the degree of basement-membrane collagen that surrounds tumor capillaries, especially as they varied across different tumor phenotypes [110]. SHG has likewise been used in the visualization of enzyme-degradable Qdot formulations through synthetic collagen gels *in vitro* [111]. With *in vivo* imaging, one study correlated SHG with local vascular perfusion, and found that collagen deposition and general fibro-inflammation induces high interstitial pressures and vascular collapse in pancreatic cancer [112]. Even for un-encapsulated small molecule drugs such as gemcitabine, this desmoplastic reaction created a substantial barrier to tumoral drug accumulation, and could be ameliorated using recombinant hyaluronidase to degrade ECM [112]. Alternatively, treatment with TGFβ inhibitor has been shown to especially improve the penetration of large (>30 nm) NPs in pancreatic tumors [50], through increased recruitment of perivascular cells to tumor vasculature, improved vascular perfusion, and reduced collagen I deposition [113]. Other treatments aimed at overcoming stromal barriers include ultrasound; vasoactive treatments such as relaxin, thrombin and angiotensin II; heparanase inhibitor; treatment with degradative enzymes including hyaluronidase and collagenase; inhibition of kinases including VEGF and PDGF (platelet derived growth factor); and targeting cancer associated fibroblasts through FAP (fibroblast activation protein) [102]. Outside of cancer applications, IVM of ECM features and collagen deposition has been useful in inflammatory diseases like dermatitis [114], atherosclerosis [115] or models of arterial injury [116]. In the latter, SHG was used to visualize collagen deposition; in contrast to the studies in desmoplastic cancers, collagen deposition actually correlated with local NP delivery to macrophages at sites of endovascular injury and wound response [116]. Going forward, stromal and ECM imaging will be important in guiding the development of NPs and adjuvant strategies that overcome physicochemical delivery barriers.

2.5. What governs NP clearance and toxicity?

Although *in vivo* imaging has elucidated details of NP behavior at target sites, typically >95% of injected NPs are sequestered or cleared from the body via MPS and the renal system and fail to actually accumulate in the tumor [12]. 40–50% of NPs are typically excreted, and the remaining may accumulate in the body for weeks or longer, especially for NPs composed of non-biodegradable inorganic materials [117]. Although long-term safety has been demonstrated for many NPs, it is nevertheless critical to understand their transport and biotransformation in off-target tissues [117]. To this end, IVM approaches provide unique insight into biological mechanisms of NP clearance and ways to improve or minimize it.

Cellular mechanisms of systemic clearance: The liver and kidney comprise two of the most important organs for drug and NP clearance, and fluorescence imaging of both has been useful for studying cellular clearance mechanisms of NPs and model therapeutic payloads. While NPs or large proteins have been found to accumulate in liver hepatocytes via endocytosis, negatively-charged Qdots (~4 nm diameter) are completely absent from hepatocytes and instead accumulate in resident liver phagocytes (Kupffer cells) and liver sinusoidal endothelium [40]. Similarly, larger (100 nm diameter) mesoporous silica NPs also lack hepatocyte uptake and rapidly aggregate within the sinusoid [40]. In contrast, the model fluorescent small molecules rhodamine-123 and fluorescein are readily taken up by hepatocytes and excreted into bile [40]. Non-fluorescent derivatives of fluorescein have been used with IVM to monitor metabolism into fluorescent byproducts in hepatocytes, which can be done at sufficiently high resolution to discern nuclear versus cytoplasmic localization [118]. Drug transport studies in the kidney [32] show early Qdot accumulation in the peritubular capillaries and glomerular arterioles, followed by transport to fenestrated glomerular endothelium and eventual uptake by mesangial cells. In contrast to negatively-charged Qdots, cationic Qdots readily pass through the anionic glomerular basement membrane and are rapidly excreted into urine [32]. In both studies, multiphoton IVM was combined with fluorescence lifetime imaging microscopy (FLIM) to selectively image Qdots, which have long fluorescence lifetimes compared to organic dyes and autofluorescent tissue. Other studies have monitored transport of different folic-acid conjugates through the kidney. Clever comparison of conjugates labeled with dyes that are either pH-sensitive (fluorescein) or pH-insensitive (Texas Red) allowed inference of pH in endocytic compartments as the drug transcytoses from apical to basal surface of proximal tubule cells [119]. Taken together, these results bear relevance to renal and hepatic toxicity, manipulating clearance rates through NP engineering, and predicting drug-drug interactions.

Imaging molecular transporter activity: Drug efflux pumps are a class of transmembrane transporters that most prominently include P-gp/MDR1, and are found at high levels in key barriers of the body such as the blood-brain barrier and intestine, along with sites of drug clearance including the renal proximal tubule and the liver. Efflux pumps regulate systemic PK of multiple drugs, their upregulation or inhibition can impact the bioavailability of co-administered drugs, and their upregulation also contributes to drug resistance (as discussed above). Drug efflux analysis is a natural application of IVM, considering many fluorescent compounds themselves are efficient efflux pump substrates. As a P-gp substrate, Rhodamine-123 has been used with IVM to assess P-gp function in hepatocytes and the impairment of said function by co-administered drugs known to interact with P-gp [120,121]. Such analysis has shown not just how P-gp inhibition influences systemic PK, but also how impaired drug efflux enhances drug accumulation in individual hepatocytes and slows drug clearance to the bile [120]. Fluorescent drugs and dyes (including borondipyrromethene, BODIPY) serve as transport markers for an array of efflux proteins, including ABCB1/MDR1/P-gp (calcein-AM; BODIPY labeled forskolin, verapamil, vinblastine, prazosin, paclitaxel, eribulin, daunorubicin, doxorubicin, hoechst33342, BCECF-AM, Rhodamine-123); ABCC1 (calcein-AM; fluro-4-AM; mitxantrone; BCECF-AM; daunorubicin; doxorubicin; fluo-3); ABCC2 (doxorubicin; carboxy-2′,7′-dichlorofluorescein); ABCC4 (BCECF); ABCC5 (fluorescein; 5-chloromethylfluorescein diacetate [CMFDA], BCECF); and ABCG2 (mitoxantrone; hoechst33342) [122]. IVM application to drug efflux is of particular relevance to nano-formulations, considering i) nano-encapsulation has been frequently used as a strategy to bypass drug efflux pump action [123]; ii) many of the above-listed drugs have served as NP payload for therapy; iii) NP vehicles and degradation products can influence efflux pump expression and are themselves pump substrates [124]; and iv) nano-encapsulation has been used to efficiently deliver P-gp inhibitors, which exhibit notoriously poor PK properties as un-encapsulated compounds, to resistant tumor cells [56].

2.6. What clinical lessons have we learned from IVM imaging

In vivo imaging may offer insight into how nano-materials and drugs apply to biological systems, yet it can be a challenge to translate understanding at the microscopic level into the clinic. As a preclinical tool, IVM helps guide the development of new NPs and corresponding NP-targeting or adjuvant strategies. Beyond this, IVM clinically translates in two principal manners: i) through clinical IVM systems being developed for dermatology, endoscopy, and intra-operative applications; and ii) through guiding implementation and interpretation of clinical MRI and PET/CT in patients.

Clinical IVM systems include endoscopic confocal fluorescence [125] and multiphoton [126] microscope systems that have been used for various measurements including capillary structure, perfusion, and permeability [125]. Confocal endomicroscopy is additionally used to examine various tissues for dysplasia, including the cervix [127], lung [128], along with colon and rectum [129], and is available through commercial vendors (for example, Mauno Kea Technologies). Intra-operative confocal microscopy is also performed to evaluate tumor margins, for example in brain [130] and urologic [131] cancers using 5-aminolevulinic acid. Targeted fluorescent molecular probes for instance targeting the cancer markers prostate-specific membrane antigen (PSMA) [132] and cathepsins [133] enable intraoperative fluorescence imaging at the time of tumor resection to identify tumor margins. Bedside IVM systems have also been developed for cutaneous imaging in melanoma, and have been primarily useful for quantifying the tumor vasculature's structure, permeability, and perfusion [134]. IVM has not been widely used for NP imaging in the clinic; however, the progress in endoscopic and laparoscopic fluorescence imaging [126,132,133] combined with the demonstrated safety and routine use of various NPs and fluorescent dyes in patients suggests that such applications are feasible.

Clinical NP imaging is possible using magnetic iron oxide NPs such as the dextran-coated ferumoxytol (Feraheme), which has been approved by the FDA for the treatment of anemia. Ferumoxytol is a long-circulating NP that accumulates in phagocytic immune cells and in solid tumors via the EPR effect, and various studies have used it to image abnormal vasculature in stroke [135]; inflammation in type I diabetes [136]; lymph node metastasis detection [137,138]; and heterogeneous EPR effects in solid xenograft tumors [54]. In the latter example, EPR effects measured by ferumoxytol-MRI were able to accurately predict the tumoral accumulation and response to a subsequently administered taxane-NP across cohorts of xenograft mouse models [54] (Fig. 8). In effect, this study shows the potential for companion-imaging approaches to select patients into therapeutic NP trials. NPs have also been developed for PET/CT imaging, often based on modified magnetic NPs including ferumoxytol [139], and have the potential for clinical application but as of yet their use has been fairly restricted in the clinic. For example, only recently have pilot studies been performed that use PET/CT to examine tumor uptake of a drug-loaded liposome, in one case a ^{64}Cu-doped HER2-targeting liposomal doxorubicin for breast cancer treatment [28]. Cyclophosphamide adjuvant was used to improve tumoral liposome accumulation (also monitored by PET/CT in patients) [140]. As another example, RGD-functionalized ^{124}I silica NPs were safely imaged by PET/CT in cancer patients, which in one instance revealed NP accumulation at the margin but not in the core of a hepatic metastasis [141]. Overall, IVM can provide insight into the molecular and cellular mechanisms that govern NP accumulation, along with what the time-scales of those mechanisms are. It thus provides important context for the interpretation of the lower resolution clinical imaging modalities, and subsequently guides the dosing, timing, and acquisition parameters for optimal and interpretable results.

2.7. Why use IVM to study new NP formulations?

High resolution and multicolor capabilities allow IVM to capture a large amount of information regarding the behavior of NPs and their impact on disease biology (Box 1). By directly imaging *in vivo*, IVM avoids many artifacts and complex variables associated with modeling NP behavior *in vitro*, and allows observations of NP behavior and biological response just as they happen within naturally complex microenvironments. As discussed further below, improvements in imaging stability, resolution, multicolor imaging, and biological modeling have led to increasingly rich datasets that capture the spatiotemporal behavior of thousands of cells over the course of hours, days, and weeks. To interpret this often highly quantitative data, machine-learning and multivariate statistical approaches have been developed for efficiently deriving new biological insight. In fact, one of the most powerful applications of IVM is its ability to statistically correlate multiple image features with each other over time, and in the case of NP imaging this includes directly observing the relationship between NP delivery and its impact on subsequent cell behavior at the single-cell level. For instance, imaging has been used to monitor the *in vivo* delivery of NPs to phagocytes and monitor their migratory response to NP-encapsulated piceatannol, which blocks integrin adhesion signaling in phagocytes [90]. In this study, IVM was useful in identifying not just what immunologically-defined neutrophil populations accumulated NPs, but what their migratory, cell signaling, morphological, and intravascular adhesion behaviors were at the time of treatment. Time-lapse measurements then showed how loss of adhesion, commencement of cell rolling, and morphological cell rounding all occurred in neutrophils that lined inflamed vasculature and accumulated NP. Because this study did not simultaneously measure PK/PD but rather examined them in separate serial experiments, it was not possible to quantify relationships between heterogeneous NP accumulation and resulting migratory changes, which may be especially important in more heterogeneous disease models or when examining off-target or off-site drug effects. As discussed further above, other studies have performed simultaneous PK/PD imaging, which reveal spatial relationships between perivascular NP accumulation and the effects on both neighboring and further extravascular tumor cells [55,56].

In the context of diseases related to neo-vascularization such as cancer and ophthalmic disorders including macular degeneration, vascular structure is often itself a PD response, thus making *in vivo* imaging a natural approach for combined PK/PD analysis. For instance in application to corneal neo-vascularization, IVM was used to image the elution of a model fluorescent drug, doxycycline, from its polymeric nano-wafer scaffold [38]. After establishing that the wafer could release drug gradually over the course of 24 hours, PD imaging of corneal vascularization was then used to select an optimal VEGFR kinase inhibitor. Additional IVM was performed to monitor vascularization and treatment thereof in a corneal burn model [38]. In another example, NPs comprised of a silica core, gold shell, and VEGF targeting ligand were used to photo-thermally ablate tumor vasculature, and the success of this treatment was monitored by IVM [142]. PK/PD imaging can also be applied to monitor the combined delivery and effect of adoptive cell therapies, such as was done with fluorescent alginate-encapsulated cells that secrete the anti-angiogenic agent endostatin [143]. In this work, IVM simultaneously visualized the local deposition of a cellular implant and its impact on local vasculature. Although nanomedicines have routinely demonstrated clinical safety benefits compared to traditional therapies, improvements in efficacy have been stubbornly difficult to consistently prove [11]. Thus a major current challenge in nanomedicine has been to understand barriers to efficacy. Especially for nano-encapsulated medicines, both the delivery and drug action at target tissue sites can be highly heterogeneous and may fail for multiple reasons. IVM enables direct and integrated insight into the complexity of NP biological activity, and with the help of appropriate image processing, computational modeling, and statistical analysis tools, microscopy has the potential to efficiently identify key factors in the success and failure of new nanomedicines.

3. The nuts and bolts of IVM nanoparticle imaging

Several recent publications have summarized the integral components of intra-vital microscopic imaging experiments in mouse models [109, 144–152]. Rather than the reiterating the basic aspect, the reader is referred to practical summaries of window chamber models [153], and device setups [151]. The sections below will therefore focus on unique applications to imaging NPs in vivo.

3.1. Imaging cellular-level pharmacokinetics (PK) and pharmacodynamics (PD)

For a given fluorescent drug or NP system, time-lapse IVM enables concerted measurement of both the kinetics of drug transport and the action of the drug at various targets in the body. Although specific aspects of NP pharmacokinetics are discussed as applications further below, in principal the basic features of L-ADME (Liberation, which is the process of drug release from its NP vehicle, along with Absorption, Distribution, Metabolism, and Excretion) can be tracked by IVM and complimentary fluorescence methods, with the general exception of metabolism. Measurement of drug metabolite formation generally requires analytical methods such as liquid chromatography - tandem mass spectrometry (LC/MS/MS), although certain fluorogenic reactions have been designed in limited applications for monitoring metabolic bi-products *in vivo* [118]. With this caveat, IVM enables PK understanding at a much greater temporal and spatial resolution than is typical for traditional PK modeling, and can reveal drug uptake at sub-cellular resolution. Drug PD is tightly coupled to its PK, as drug responses can be highly sensitive to concentration and timing. Furthermore, PD responses often span multiple time and length scales across myriad biological pathways. Through longitudinal multicolor imaging, IVM is thus positioned to study interconnected relationships between PK and the multiple layers of PD, beginning with drug-target binding, through downstream cellular pathway activity and response, to disease progression and outcome.

3.1.1. Optical tracking of systemic PK—In its simplest form, time-lapse IVM supports non-invasive monitoring of systemic PK with high temporal resolution, such that traditional PK parameters can be measured with the appropriate calibrations and controls that relate imaging to concentration (Fig. 1). These parameters include the peak plasma drug concentration (C_{max}), time to reach C_{max} (known as t_{max}), the lowest plasma concentration before a subsequent dose is administered (C_{min}), the volume of distribution (V_d), the elimination half life ($t_{1/2}$) and elimination rate constants (k_e), the clearance (CL), the area under the concentration curve (AUC), and the bioavailability (f) when alternative routes of administration are considered besides intravenous. Compared to traditional analysis that usually involves periodic blood draw, *in vivo* imaging is non-invasive when performed in the thin skin of the ear; allows high temporal resolution for accurate PK parameter measurement and facile detection of multi-phased PK mechanisms such as initial distribution, re-distribution, and terminal half-life; allows for multicolor imaging and simultaneous tracking of multiple NPs or drugs in the same animal; and relaxes constraints on repeat dosing or measurement in the same animal that would typically arise from serial blood collection.

Systemic PK analysis is the first step in gauging the effects of drug nano-encapsulation, and IVM has been used to demonstrate that liposomal daunorubicin exhibits an extended plasma half-life compared to its unencapsulated counterpart [85], or more recently that polymeric encapsulation of a cisplatin-related prodrug exhibits a substantially longer plasma half-life [55] compared to un-encapsulated fluorescent cisplatin- or carboplatin- derived Pt imaging agents [154]. Consistent with *in vitro* behaviors, *in vivo* imaging has also confirmed the presence of an initial burst-phase of payload release immediately upon injection followed by more gradual release profiles for several formulations, which may be attributed to altered stability and thermodynamics upon NP dilution and serum exposure [36,55].

IVM has the potential to detect microscopic behaviors of NPs, even as they circulate in blood. For instance, imaging has shown how red blood cells influence nano- and micro-particle margination in flow through capillary beds [35], which is more pronounced for larger (>100 nm) particles [46] compared to smaller NPs. Such margination impacts fluid mechanics and stresses experienced by the particles, is a function of both NP size and shape, and may actually be beneficial for extravasation at target sites [35]. IVM furthermore supports measurement of NP aggregation and clotting processes, especially as they occur in microvasculature, for instance as was seen with cationic siRNA-loaded hydrogel NPs [155]. Overall, the extended stability, low plasma clearance, and controlled extravasation all contribute to an increased ability for NPs to deliver sustained levels of drug to target cells.

3.1.2. Imaging drug binding—The most proximal pharmacodynamic effect of a drug can generally be defined as the biochemical reaction of the drug binding to its biological target (or off-target), and developments in optical capabilities combined with selective fluorescent drug-conjugates have made it possible to directly image NP or drug binding to its molecular target *in vivo*. Recent fluorescent-drug conjugates showing selective target binding by IVM include ibrutinib-BODIPY targeting Bruton’s tyrosine kinase (BTK) [156,157], olaparib-BODIPY targeting poly-ADP ribose polymerase (PARP) [158], folate-Alexa488 targeting folate receptors (FR) [159], and the polypeptide exendin-4-VT750 targeting glucagon-like peptide 1 (GLP-1) in pancreatic β-cells [160]. Fluorophore-antibody conjugates are also used for IVM applications [161], for example to image tumor cells that over-express particular molecular targets [162–165], various immune-cell populations [166,167], and thrombus components including platelets and clotting factors [168].

Drug binding can be inferred several ways by IVM. At the simplest and least accurate level, fluorescent drug retention within target cells may be interpreted as drug binding. This approach depends on appropriate controls, such as competition experiments with non-fluorescent drug, and works best when the drug has a known target with predictable cellular or subcellular localization, such as in the nucleus (as with the PARP inhibitor olaparib). Accuracy of drug-binding measurement is improved by using animal models with transgenic fluorescent target proteins. For instance, variable transgenic expression of BTK in originally non-expressing tumor cells allows for robust co-localization analysis [156,157]. For NP vehicles themselves, *in vivo* co-localization analysis is possible for measuring NP uptake into fluorescently-tagged subcellular compartments such as endosomes or lysosomes [48]. For most accurate IVM drug binding measurements, new fluorescence anisotropy methods have been developed to visualize the binding of fluorescent-drug conjugates to their larger (and more anisotropic) protein targets [169]. Fluorescence intensity, anisotropy, and co-localization with reporter proteins collectively discern not just how much drug is accumulating in individual cells or subcellular compartments, but also how much drug-target is expressed, how much drug is binding to its target, and how much drug is binding to off-target proteins.

3.1.3. Fluorescent genetic reporters of tumor cell response—

Subcellular resolution imaging not only measures fluorescent NP uptake and action at the single-cell level, but also enables simultaneous observation of fluorescent genetic reporters for understanding which cell types accumulate NPs and how they biologically respond. Perhaps at the simplest level, fluorescent genetic reporters can indicate the effects of nucleic-acid based treatments including viral gene therapy [170], siRNA-loaded NPs [171], and more recently CRISPR/Cas9 based NPs [172], that are designed to either activate or silence the expression of particular genes. IVM helps define spatial and temporal patterns of gene expression responses [173], and combined use in reporter GEMMs allows for assessment of gene expression in specific target cell populations such as macrophage progenitors [174] or myeloid cells in a tumor’s draining lymph node [175].

Anti-mitotic and cytotoxic therapy response can be visualized using various fluorescent reporter systems. Key examples in IVM include measuring cell-cycle using the GFP/RFP FUCCI system [58,176]; chromosomal segregation and mis-segregation during mitosis using histone 2B [55,57]; DNA damage response by visualizing punctate nuclear accumulation of the DNA damage response protein 53BP1 [154,177]; apoptosis by imaging mitochondrial outer membrane permeabilization (MOMP) [178]; and autophagy as seen through GFP-LC3 localization to autophagosomal vacuoles [179]. Additional fluorescent reporters relevant to cytotoxic response show promise as demonstrated by *in vitro* use, including reporters of homologous recombination (Rad52 [180]) and cell stress using p53 [181].

Kinases are a major class of drug targets in oncology and inflammation, and nanoencapsulated kinase inhibitors show promising therapeutic index [182]. FRET- and Fluorescence Lifetime Imaging Microscopy (FLIM)-FRET reporter systems have been developed for real-time monitoring of *in vivo* kinase activity at high spatiotemporal resolution. For instance, a FLIM-FRET biosensor of Src activity was monitored in response to the Src inhibitor dasatinib, showing *in vivo* drug efficacy and kinetics of Src inhibition, distinct response depending on proximity to vasculature, along with regions with poor drug penetrance in vivo, and thus poor drug-targeting efficacy [183]. In other examples, FRET-reporters of the mitogenic Erk pathway identify influence of local fibroblasts in mediating drug resistance [184], and highlight heterogeneity of Erk activity during cancer development in a GEMM [185]. Additional FRET [186–188] and nuclear translocation-based [189,190] fluorescent reporter systems have been developed and demonstrated *in vitro* for targets including the mitogenic kinases Erk, Akt, PKA; the stress-response kinases Jnk and p38; and the DNA damage response kinases ATM and ATR, among others. As for many FRET-reporter systems, application to IVM is promising but challenging because signal-to-noise is often lower than 20%.

3.1.4. Cell migration, host-cell interaction, and cell fate—*Cell migration, movement in and out of blood vessels, and cell-cell interactions* including through immunological synapses are all key processes of inflammation, metastasis, and drug response and can be measured by IVM. Recent work has used time-lapse imaging to observe tumor interactions with ECM [191] and with microvasculature [64]. Furthermore, Rho-family GTPases Rac1, Cdc42, & RhoA play key roles in governing cellular motility, and their activity can be visualized by FRET-reporter systems and correlated with *in vivo* cell migration [192]. In the context of drug response, IVM has helped reveal how physical cell protrusions and interactions with vasculature change in response to anti-angiogenic therapies [64]. Other work has shown cancer cells in S/G2/M phase to be more invasive [193]. Many more migration-related reporters have been described and demonstrated *in vitro*, including for activity of metalloproteinases MT1-MMP [194] and ADAM17 [195], both of which importantly govern cell migration and response to therapeutics [196,197].

IVM of host-cell behavior, such as T-cell [198] and dendritic cell [199] migration dynamics in the lymph node, has been ongoing for over a decade using fluorescent genetic reporters of particular cell populations [200]. IVM enables useful 3D mapping of dynamic multicellular structures, for instance of neuronal pathways [201]; cell-cell communication can be observed by dynamics of cell-cell contact, for instance among antigen-presenting cells and pathogens in the lung [42]; and even intercellular transfer of microvesicles from one cell to another [202,203] are visualized. For greater versatility, fluorescent cell populations can be adoptively transferred, as has been done with GFP-expressing granulocyte macrophage progenitor cells (GMPs) [174]. Similarly, cells that have been labeled *ex vivo* with fluorescent NPs including dextran NPs [204,205], Qdots [206], or more recently NIR-emitting nanodiamonds [207] can be transferred and imaged by IVM. In the context of therapeutic NP delivery, reporter GEMMs containing CX3CR1$^{GFP/+}$ phagocytes, including dendritic cells and macrophages, have been used with IVM to directly observe NP uptake in tumor-associated phagocyte populations and map the dependency on vascular proximity [54,55]. Ultimately, the advent of CRISPR/Cas genome engineering in mice promises to greatly accelerate our ability to generate fluorescent reporter GEMMs for specific immune, stromal, and cancer cell populations for IVM applications [208].

Cell fate: Several strategies have recently been developed to better delineate neighboring cells, trace cell lineage, and monitor clonal outgrowth. Brainbow GEMMs [209] and the LeGO lentiviral system [210] are based on stochastic expression of multiple fluorescent proteins, thus leading to multicolor cell populations [201]. In application to drug response, LeGO enables selective labeling and monitoring of drug resistant cell lines [211], and furthermore allows automated clonal tracking of single tumor cells within a xenograft by IVM [212,213]. Brainbow-supported clonal analysis of hematopoietic stem and progenitor cells [214] and antibody affinity maturation in germinal centers [215] has great potential in application to therapies with target/off-target hematological toxicity or immunogenicity. Photoconvertible fluorescent proteins such as in the Kaede-reporter GEMM [216] or the

NIR lipid dye DiR [217] represent tools for cell tracking with IVM, for instance useful for in vivo pathogen labeling [218] or tracking metastastic dissemination [146,147].

3.1.5. Physiological features of the microenvironment—IVM has long been used to measure vascular structure and drug diffusion into surrounding tissue [219,220], including for NPs such as liposomal doxorubicin that benefit from EPR effects [221]. ECM imaging via multiphoton SHG [222] enables visualization of ECM structures including collagen fibers, which influence cell behavior [191] and drug delivery [112]. SHG also enables visualization of striated myosin and has been used to monitor sarcomere length during statin treatment [223]. Less commonly used, in part do to requirement of longer wavelength excitation source (~1300 nm), third harmonic generation (THG) enables visualization of refractive index mismatches within tissue, which illuminates blood vessel walls, blood cells and thus blood flow, nerve fibers and myelin [224], phagocyte migration, and cell nuclei in some cases [225].

Vascular structure, perfusion, and permeability continue to be key features captured by IVM, and IVM studies have been useful in parsing the influence of various cell populations including perivascular VEGF+ macrophages [64]; therapeutic adjuvants such as anti-VEGF treatment [226], radiation [227], ultrasound [228], and hyperthermia [47,229,230]; and NP physicochemical features such as size [50,219] and shape [231] impact transport from vasculature to the target tissue. Reporter GEMMs enable clear and simultaneous visualization of vascularity, for instance using Tie2-GFP GEMMs [230], and neighboring cell populations. As an example, a two-color GEMM that ubiquitously expresses membrane-anchored RFP, including in the endothelium, and GFP in CX3CR1+ phagocytes, was used to visualize NP transport from tumor vasculature to adjacent perivascular phagocytic cells [54]. Fluorescent dextran conjugates of various molecular weight are often used to measure vessel permeability in both cancer and inflammation, as was recently done in study of local tissue heating [230], local macrophage accumulation [64], allergan-induced permeability from IgE release [232], and interferon-gamma induced permeability in a model of colitis [233]. Increasing IVM resolution and stability have enabled much greater mechanistic insight into the causes of macromolecular or NP extravasation, with recent insight into the role of subcellular tumor-cell protrusions into vascular space [64] and highly dynamic bursts of NP extravasation that last under 30 min for smaller NPs [30].

3.2. Intravital microscopy (IVM) techniques

IVM often requires a diverse set of tools and approaches depending on the scientific question being addressed, with factors such as anatomical site, imaging time-scale, resolution requirement, and throughput all influencing the optimal setup. Here we focus on mouse imaging, although microscopy of lower organisms such as zebrafish and drosophila is common and is reviewed elsewhere [234–236], including for application to high-throughput drug development [237,238] and nanomaterial toxicology [239]. In its simplest form, IVM in mice can be performed on the thin skin of the ear, which can be taped flat to the heated microscope stage. This approach is fast, reliable, and enables facile assessment of PK and extravasation in healthy model tissue. The mouse ear shares complimentary melanocyte distribution compared to humans, and therefore serves as a useful site for intradermal melanoma xenograft implantation and subsequent imaging studies [240]. However, more invasive surgical approaches are generally required for imaging deeper in tissue be it by window chambers or intraoperative/endoscopic orthotopic imaging.

3.2.1. Window chambers—Surgically implanted window chambers are routinely used in IVM to enable longitudinal imaging over days and weeks with relatively little setup, tissue damage, inflammation, or animal discomfort caused after tissue has recovered from the initial surgery [145]. In many ways, the skinfold chamber is the simplest and most reliable, versatile method for making stable and clear images. This window consists of a metal bracket sutured to a fold of skin, generally on the mouse back, with a glass cover slip replaced over a surgically removed section of skin, and is typically used for imaging subcutaneous tumor models, lymph nodes, and mammary fat pad tumors when placed over the fat pad. Implantation into deep dermis helps avoid artificially constrained pseudo-2D growth, and temperature effects can be ameliorated by heated housing facility and environmental imaging chambers. The biggest benefit of the skinfold approach is the ability to mount the chamber and tissue to the microscope stage and prevent nearly all motion artifact from animal respiration and digestion. Compared to the dorsal skinfold chamber, mammary imaging windows are smaller to accommodate more constrained anatomy, but successful use is nevertheless more difficult. As an alternative, elizabethan-collared metal frame windows between the skin and mammary fat pad offer less intrusive and obstructive surgery but at the cost of motion stabilization. Abdominal imaging windows are similar in structure to the mammary window but larger, and are useful for imaging abdominal organs including the intestine [241], liver [146], kidney [145]. spleen [145], pancreas [145], and ovary [242]. Due to extensive organ movement, it is frequently necessary to immobilize target imaging sites to the window with cyanoacrylate glue, Vetbond tissue adhesive, surgical suturing to the abdominal wall, and also to prevent the window from being occluded by fluid pooling.

Inverted microscopes are best for mammary and abdominal window imaging to again minimize motion artifact, although imperfect immobilization solutions for upright setups have been described. In contrast, the dorsal skinfold chamber works with both upright and inverted microscopes. Cranial imaging windows (CIW) are implemented for either the frontal or occipital lobe using one of two approaches. The chronic CIW comprises a craniotomy followed by a glued window, and the thin skulled window consists of a micro-drilled skull thinning, which minimizes microenvironmental disturbances within the skull. Compared to the thin skull method, the CIW is associated with increased spine turnover and glial activation [243].

Although effective, many surgical approaches including window chamber implantations are still invasive, unavoidably inflammatory to a degree, and require anesthetics for imaging which is especially problematic for neurological studies. Recent work has attempted to miniaturize optics and electronics for implanting imaging systems that eliminate the need for anesthesia [244]. Several imaging methods have been developed, particularly for NPs, that enable deep-tissue imaging without the need for surgery, including ultrasound, luminescence, magnetic resonance, and CT; nevertheless, the resolution and ability to imaging multiple distinct channels comes nowhere near to what is achievable by confocal and multiphoton approaches. Long-term imaging of the heart and lung still remains a challenge, and new fluorophore schemes and surgical approaches are being developed to reach deep tissue [245–249].

3.2.2. Orthotopic imaging and immobilization—In the absence of surgically implanted windows, IVM supports orthotopic imaging at a wide range of anatomical sites. Orthotopic imaging typically occurs during terminal non-survival imaging sessions, although intra-operative survival procedures are also possible. Non-survival procedures allow for the possibility of more invasive surgery, for instance involving opening the rib cage for access to the lung and heart [247], and orthotopic sites can also be surgically externalized, manipulated, and even mounted on a heated, compliant substrate for stable and flexible imaging. Externalization procedures are most successful for abdominal organs such as the intestine [54], liver, and pancreas, or superficial tissue structures including tumors of the mammary fat pad [158].

Desiccation, thermal regulation, damaged vasculature, and movement are especially important factors to address when performing IVM surgeries. Tissue dessication and evaporative heat loss can be addressed by applying warm isotonic Ringer’s solution and minimizing the surface area of exposed tissue, for instance by minimizing surgical incisions, organ externalization, and even by sealing exposed areas using plastic wrap [250]. Vascular damage can be minimized by careful organ manipulation using damp saline swabs, blunt tissue forceps, and microcautery when necessary. Once externalized or manipulated into place, tissue can be stabilized by using a small suction window that diffusely applies a small vacuum pressure around its window frame [249,251], as demonstrated for the pancreas [250], lung [252] and heart [249]. As a caveat, excess negative pressure has the potential to artifactually disrupt tissue physiology, for example through pressure-induced vessel collapse. Narrow-shaped stick objectives, especially when combined with window-suction devices [249] and micro-manipulation stages [179], are versatile and allow for stable imaging in deep anatomical locations. As an alternative to suction, parenchyma can be glued onto the imaging frame or cover slip [253,254]: however, this approach can lead to autofluorescence [45], requires a relatively large flat outward surface for immobilization compared to stick objectives, and limits the ability for repositioning and intentional tissue movement [251]. Real-time prospective gating to match image acquisition with rhythmic beating or breathing also minimizes the movement between image frames, as done for instance to visualize single-sarcomere movement in the beating heart [247,255]. In the same vein, synchronized respiration and holder further improve stable acquisition [256]. Heuristic computational approaches can be taken to optimize the time it takes to acquire images [257]. Although discussion of microscope optics extends beyond the scope of this review, several adjustments including objective collars [258], real-time wavefront detection and feedback [259,260], and increased inter-pinhole distance [261] all correct aberration in thick specimens and have been developed for deep-tissue IVM applications. IVM often involves imaging structures that are large and bright next to structures that are equally important yet small and dim, for example in the case of neuron nuclear bodies and their thin axon processes; high-dynamic-range setups have been described to simultaneously capture these disparate features [262]. Photobleaching and phototoxicity are also prominent issues in time-lapse IVM, and light-sheet microscopy successfully addresses these issues but still does not readily accommodate specimens larger than an embryo [263,264]. Overall, anatomical immobilization, surgical manipulation, optical stabilization, and gated acquisition combine to improve IVM image quality.

3.2.3. Image processing and analysis—Compared to *in vitro* microscopy, IVM data is complex both in terms of artifacts related to tissue autofluorescence, scattering, and motion, and in terms of the complex biology of multiple cell types and structures behaving dynamically in three dimensions. To deal with these issues, a host of computational methods have been developed for refining and interpreting IVM datasets. Image pre-processing allows for the automated removal of motion artifacts including image translation and distortion from tissue compression or expansion [245,248], and available standalone and plugin software enable automated image filtering based on motion artifact [265,266]. Fluorescence attenuation from tissue scattering depends on the wavelength and optical tissue properties, and corresponding correction techniques have been developed [267] that complement noise-correcting methods in standard image analysis software platforms including the academic/nonprofit lmageJ [268] and Cell Profiler [269] platforms, along with commercially offered Matlab (Mathworks) and Imaris (Bitplane).

Once IVM data has been pre-processed to remove noise, motion, and scattering artifacts, a major challenge remains to interpret the biological features of the data: what are the shapes and movements of cells, vessels, and NPs over time?; what limits selective NP transport to its target site?; and how does NP transport correlate with response at the single-cell and macroscopic/clinical level? Manual image analysis is often limited in capability, time-consuming, and prone to bias, and thus automated computational routines offer distinct advantages. For IVM, the first step in computational analysis typically involves automated or semi-automated segmentation of different cell-types and vessels using thresholding algorithms, and the most accurate applications contain an ability to manually train and improve the segmentation parameters using iterative machine-learning [58]. Especially for 3D images, segmentation can be computationally intensive and require many hours to complete, even with the use of a highly parallelized scientific computing cluster. To address this issue, heuristic algorithms have been developed for rapid nuclear segmentation [270], and resulting positional information enables high-throughput quantification of embryonic development [271] and pathological cell invasion [197,272]. Once cells have been segmented, intensity of fluorescent drugs [158,273] and NPs [55] can be quantified on a single-cell basis; phenotypes of fluorescent genetic reporters can be used to sub-classify individual cells, for example according to cell-cycle and mitotic catastrophe based on FUCCI and histone reporters [58]; and statistical relationships between cell phenotype and the local microenvironment can be calculated [55]. Segmentation of vasculature is highly relevant to drug transport, and various programs exist to efficiently map vessels and analysis properties such as diameter, branching features, and interconnectedness [274]. IVM of dyes, particles, and cells in microvasculature, including through THG imaging, also enables direct measurement of fluid flow and single-cell movement along capillary walls. These features can then be mapped to vessel structure information to glean an array of mechanical properties [134,275,276]. Computational studies of vascular perfusion [277] and its effect on tumor growth [278] or thrombosis [279] are all examples of IVM data-driven modeling. In the context of drug delivery, vascular features can be combined with single-cell segmentation and IVM drug imaging to map the reaction/diffusion processes of drug transport out of vessels and into individual cells [30,54,158] or even within subcellular compartments of individual cells [280].

Future work will likely combine single-cell PK measurements and IVM datasets with complimentary ex vivo measurements and computational modeling of biological response pathways. Towards that direction, one recent study has integrated IVM measurements with immunohistochemistry of the same tissue for greater biological context [281], and new methods for high-content immunofluorescence [282,283], multiplexed mass spectrometry imaging [284], and *in situ* RNA sequencing [285] will be powerful complementary tools. Computational modeling of complex and stochastic biological networks has proven useful in understanding cell behavior and drug response, for instance in the context of biomechanical influences on cell signaling and behavior [286]; complex intracellular networks of kinase [287–289] and/or transcriptional activity [290]; metabolic networks [291,292]; reaction/diffusion processes of receptor signaling and antibody therapies [272]; dynamic feedback and PD response [293,294]; along with multi-scale and agent-based models of multicellular behavior [295,296]. In one recent example, IVM was used to populate a computational model of T cell migration in the lymph node, which concluded that somewhat noisy, probabilistic migration behavior actually improved the robustness of immune surveillance [297]. Recent IVM advances have led to the creation of highly rich, quantitative datasets that are of sufficient resolution to benefit enormously from computational tools for i) mapping 3D cellular distributions, vessel structures, and spatial/morphological relationships; ii) classifying cell and vessel populations based on imaging phenotypes; ii) tracking single-cell movement over time; and iii) simulating the combined pharmacokinetics and pharmacodynamics of drugs moving from vessels to individual cells.

3.3. Creating fluorescent NP systems

Recent advances have expanded the range of tools available for fluorescently labeling NPs for IVM applications, yet with each strategy comes with trade-offs in terms of versatility, stability, and sensitivity. Compared to *in vitro* imaging, IVM often requires short exposure times to capture rapid cellular dynamics overcome motion artifacts from animal movement. Thus quantum yield, extinction coefficient, dye concentration and non-leachability represent especially important considerations (Figs. 3, 4). Dynamic *in vivo* processes may occur on the timescale of hours, and the inherent 3D nature of these processes typically requires confocal z-stack imaging (Fig. 1). As a result, extended illumination places a high demand on fluorophore photostability. Generally, BODIPY derivatives [298], silicon rhodamine [299] and Alexa Fluor dyes such as Alexa488 exhibit superior environmental robustness and photobleaching compared to alternative dyes such as Oregon green, the bulkier cyanine-based dyes (Cy), and especially fluorescein [300] (Fig. 4). Secondly, *in vivo* microscopy generally requires fluorescent signals to penetrate through superficial tissues and anatomical structures, especially for orthotopic sites, and tissue scattering increases with decreasing wavelength of light. Consequently, development of two-photon excitable and near-infrared emitting fluorophores have been of particular value, although shorter wavelength fluorophores are still effective in many applications. Third, IVM requires successful delivery of the nanomaterial and its fluorophore to the anatomical site of interest, and influences on NP stability and pharmacokinetics need to be considered, including fluorophore charge, binding modality to the NP, hydrophobicity, lipophilicity, pH stability, and immunogenicity. Especially for fluorescent labels that are large or are themselves NPs, such as Qdots, impacts on NP size, shape, and stiffness also need to be considered. Unfortunately, very few if any systematic studies compare fluorophore performances across IVM methods, therefore indicating the need to extrapolate from the successful case studies enumerated herein.

3.3.1. Fluorophore-conjugated NPs—Appropriate NP labeling strategies depend on the NP type (Fig. 3). For polymeric micellar NPs with hydrophobic cores, the BODIPY family of dyes offers selection of effective options ranging across the emission spectrum from green to far-red, and their advantages and recent improvements have been reviewed elsewhere [301]. In general, BODIPY dyes provide excellent stability in complex and often challenging acidic or oxidative *in vivo* environments [302]; BODIPY dyes photobleach much less than other fluorophores including fluorescein [303]; BODIPYs retain efficient fluorescence across a range of lipid environments and solvent polarities [304]; and the relatively narrow excitation and emission spectra compared to other organic fluorochromes enables most common multi-channel imaging setups. Importantly, BODIPY dyes are highly hydrophobic, and computed n-octanol:water partition coefficients (cLogP) for the dye series range from 4–6.5. Recent BODIPY derivatives, such as MayaFluor, are much more hydrophilic and have improved properties for in vivo imaging [305]. Red-shifting of BODIPY fluorescence properties is accomplished through extending its pi-electron delocalization via addition of vinyl, phenyl or thiophene groups, which in turn further increases its hydrophobicity. For instance, anisole and thiophene additions to the core BODIPY structure yield the near-infrared BODIPY-630 ($\lambda_{ex}/\lambda_{em}$ = 625nm / 643nm) with a cLogP at the hydrophobic end of the spectrum (6.54). Although such high hydrophobicity detrimentally impacts solubility and behavior in aqueous physiological solutions, this feature allows for stable and efficient encapsulation within the hydrophobic cores of NPs based on block co-polymers such as poly(lactic-*co*-glycolic acid)-*b*-polyethyleneglycol (PLGA-PEG)55]. Encapsulation can be efficiently accomplished by covalent conjugation to a hydrophobic polymer such as PLGA or polylactic acid, which can then be co-encapsulated during emulsion or nano-precipitation reactions with the block co-polymer, therapeutic payload, or other imaging contrast agents. Similar hydrophobic NP anchoring has been used for SWNTs, where hydrophilic dyes (fluorescein, Cy5.5) are tethered to the SWNT surface using lipid anchors [43,306,307]. Liposomes and other lipid-based NPs are likewise suited for labeling with highly lipophilic dyes. Long-chain dialkylcarbocyanines efficiently label lipid membranes of liposomes, micellar NPs, and other biological lipid membranes including those of microvesicles and endothelial cell surfaces; DiD ($\lambda_{ex}/\lambda_{em}$ = 644nm / 665nm) and DiR ($\lambda_{ex}/\lambda_{em}$ = 750nm / 780nm) near-infrared dyes are especially useful for intravital applications [54,308], and DiR exhibits irreversible photo conversion useful for in vivo cell tracking [217].

In contrast to the above fluorophores, highly hydrophilic dyes should be used for labeling NP surfaces that are exposed to aqueous solutions. Fluorescein is often avoided due to high photobleaching and poor brightness upon cellular uptake, while rhodamine green, and to a lesser extent, Oregon green, can retain fluorescence *in vivo* and within cells [302]. Among near-infrared dyes, Vivotag-680XL, Vivotag-S 750 [54], Alexafluor dyes including Alexa647 [309], along with cyanine dyes Cy5 and Cy5.5 [90] have all been successfully used for intravital imaging applications, although Cy5 and Cy5.5 dyes exhibit more photobleaching [300]. Ultraviolet-excitable dyes such as Alexa405 and Pacific Blue have also been successfully used for intravital imaging, primarily in the context of simultaneous multicolor imaging where other fluorescent channels are already occupied, and primarily for applications such as vascular mapping where discernment of rapid dynamics or fine subcellular structures are not as essential [54,154].

3.3.2. Intrinsically fluorescent NPs

Quantum dots: As macromolecular structures, NPs have the inherent potential to accommodate larger fluorescent species including polymers and even small NPs. Qdots exhibit extremely bright fluorescence and narrow excitation and emission spectra, including in the NIR range, and thus allow for multi-channel imaging. Qdots have been extensively used for deep tissue imaging, reviewed elsewhere [310–313]; long-circulating Qdots have been useful for vasculature mapping, while molecularly targeted Qdots [314,315] have applications in selectively labeling circulating immune cell populations [316] and sensitively detecting cancer cells [317]. The lack of Qdot biodegradability increases their risk for toxicity, yet recent reports show positive safety profiles in non-human primates [318,319]. As imaging agents for therapeutic NPs, Qdots have the capability to be co-encapsulated in larger (>100nm) polymeric vesicles and core-shell polymer structures similar to those used for drug delivery, and surprising this encapsulation can enhance the Qdot fluorescence properties [320,321]. For instance, encapsulation of CdSeS/ZnS Qdots in poly(methyl methacrylate)-co-methacrylic acid (PMMA-co-MAA) increased the Qdot's quantum yield from 0.33 to 0.84, extended fluorescence decay lifetimes by blocking non-radiative decay pathways, and allowed for two-photon imaging at 2mm depths [321].

New fluorescent NP systems: Qdots and organic fluorochromes have become cost-effective, efficient, versatile, stable, and sufficiently bright tools for the vast majority of IVM applications. Nonetheless, new specialized fluorescent NP systems have been developed which show unique imaging properties and potential for some IVM applications. For instance, up-converting NPs (UCNPs) exhibit a characteristic anti-Stokes emission, which enables tissue-penetrating near-infrared excitation and multiplexing with single-photon fluorophores, reviewed elsewhere [322,323]. Primarily through pi-conjugated systems, organic polymers themselves can be used for fluorescent, luminescent, and photo-acoustic imaging applications [324–328]. Broad fluorescence spectra, short-wavelength absorption, and photothermal conversion represent challenges for these "polymer dots," although red-shifted emission spectra [329] and near-infrared emission through FRET [330] are recent improvements.

Although Qdots, UCNPs, and polymer dots exhibit theoretical advantages over traditional fluorochromes, their co-encapsulation within larger polymeric drug delivery particles [331] carries non-negligible risks of altering therapeutic NP properties including i) toxicity through introduction of non-biodegradable and/or reactive materials; ii) physicochemical properties, particularly shape, stability and stiffness through the introduction of inorganic crystals and distinct polymer systems; and iii) drug release rates, which are generally a function of the NP physicochemical properties. In some cases these alterations can be exploited. For instance, ultraviolet-degradable polymer NPs have been combined with UCNPs to allow localized degradation in vivo upon local NIR-irradiation, then leading to release of the drug cargo [332–334]. UCNP photothermal conversion has also been exploited to enable photothermal in vivo imaging and localized photothermal therapy [329].

Aggregation induced emission NPs: Fluorophore quenching is a typical problem that occurs when using excessive NP labeling concentrations [308], with Alexa Fluor dyes being less susceptible to self-quenching [300], yet certain fluorophores exhibit the unusual property of aggregation-induced emission (AIE) whereby steric restriction of intramolecular rotation in tightly packed fluorophores enables enhanced fluorescence [335]. Silole fluorogens are among the most prominent AIE dyes, and BODIPY-based dyes with AIE properties have also been described to exhibit shifted photoluminescence spectra depending on solvent polarity [336]. Multiple fluorescent AlE-dye labeled polymeric NPs have been described [337–340], often with facile synthesis in one-pot reaction schemes [341–343], and such materials have been used for intravital two-photon imaging of vasculature [344]. Relatively broad excitation and emission spectra represent a substantial limitation of this approach, however.

3.3.3. Environmentally responsive NPs—Many NP platforms have been designed to respond to local physicochemical cues at target sites for enhanced selectivity and efficiency of delivery, and numerous imaging strategies have been developed to directly visualize how such environmental cues and corresponding NP behaviors unfold in vivo. NPs have been developed to respond to a diverse range of cues, for instance including use of carbon dots to detect intracellular copper ions [345] and Qdot-encapsulated polymer to monitor temperature [346]; however, the majority of environmentally responsive systems have been directed towards measuring local pH, oxygen, and activities of enzymes such as proteases.

pH-responive NPs: Acidic pH is an important feature of hypoxic tumor environments and endosomal/lysosomal NP trafficking, and in many cases plays important roles in controlled NP degradation and drug release. pH-responsive drug loaded NPs have been extensively developed and reviewed elsewhere [347–350], and nanoencapsulation or NP-surface labeling has been a successful strategy for *in vitro* delivery of pH-sensitive dyes, including the typically cell-impermeant pyranine (8-hydroxypyrene-1,3,6-trisulfonic acid, HPTS) [351–354]. *In vivo* imaging of pH has been challenging, and the most successful strategies typically have relied on ratiometric imaging of dyes and/or Qdots with differential pH dependencies [355]. Given the success of BODIPY dyes in general for IVM, BODIPY-based pH-responsive systems may hold promise. Red / NIR aza-BODIPY (tetraarylazadipyrromethene) [356] and the green-fluorescent BODIPY-appended calix [4]arene [357] have been recently developed for improved physiological pH responsiveness. Although new dye and Qdot systems show vastly favorable transport, photobleaching and responsiveness compared to the long-used fluorescein BCECF, AM (2′,7′-Bis-(2-

Carboxyethyl)-5-(and-6)-Carboxyfluorescein, Acetoxymethyl Ester) [358], in general their application to IVM has been limited to date.

Oxygen-responsive NPs: Oxygen-responsive NPs have been developed for application to ischemic injury and cancer, where hypoxia is a frequent and relatively selective feature of the local tumor microenvironment. Oxygen-responsive NPs have been developed for over a decade [359,360], and hypoxia-induced drug delivery from NPs has can be accomplished for instance using quinone or nitroaromatics such as 2-nitroimidazole, which can reduce through biological redox reactions and lead to more rapid drug release [361]. Fluorescent probes based on similar chemistry [362,363] have enabled *in vivo* fluorescence imaging that co-localizes with tumor hypoxia markers such as HIF1-a [364]. Phosphorescent and luminescent transition-metal (Ru/Pt/Pd/lr) porphyrin systems also display oxygen responsive properties, are frequently encapsulated on silica NPs [365], within endogenously fluorescent polymer dots [366], or within polymeric NPs along with NIR reference dyes for ratiometric imaging [367,368] with up to single-particle sensitivity *in vitro* [369]. Strategies have also combined pH sensing, O_2 sensing, and reference fluorescence within a 3-color NP system [370]. *In vivo,* O_2-sensing NPs have been successfully used for sensitive imaging of zebrafish when combined with up-converting NPs (λ_{ex} = 980 nm) [371]; as macromolecular and polymer nanoencapsulated phosphorescent probes to sensitively detect hypoxia from as few as several thousand cancer cells in mouse models [372,373]; and in ratiometric fluorescent/phosphorescent biodegradable NPs for hypoxia imaging using IVM in a window-chamber xenograft model [374]. In general, O_2 sensing NPs have been successfully applied to high resolution ex vivo imaging, for instance in frozen tissue sections, and relatively low-resolution live-animal fluorescence imaging, for instance to identify macroscopic tumor features. Given such promising initial results, opportunity exists to image O_2-sensing NPs using high resolution IVM at resolutions that reveal effects from microvasculature structure, local immune infiltrate, fibrosis, cellular behaviors, and macromolecular diffusion/perfusion, all of which impacts hypoxia in malignant and infarcted tissue.

Enzymatically-triggered NP degradation has also been heavily exploited for targeted drug delivery for example through particle degradation [375] or aggregation [376] by tumor-expressed proteases, and has been reviewed elsewhere [377–379]. NIR protease-activated probes were first developed in the late nineties [380,381] and many are now commercially available. In these applications, prominent degradative enzymes include the apoptosis protease caspase-3 [382], lysosomal cathepsin peptidases [383], and collagenolytic metalloproteinases [384]. Protease activity is especially important to the biology and function of innate immune cells, and sensor-encapsulated NPs or macromolecules have been successful for imaging such cell populations in ocular inflammation (uveitis) [385], cardiovascular disease [386], and cancer [383]. Clinically, intra-operative imaging of macromolecular protease-activated probes has been recently performed to detect tumor margins [133].

3.3.4. Fluorescent labeling of therapeutic payload—Monitoring NP vehicle pharmacokinetics elucidates how nano-encapsulation alters systemic drug clearance and directs cellular uptake; nonetheless, it is often critical to additionally monitor the therapeutic NP payload itself, especially as it is gradually released from its NP vehicle, diffuses into target tissue, and exerts its biological effects. Depending on physicochemical factors including the NP release rate, the payload PK and biodistribution may diverge substantially from the NP vehicle, as has been observed with drug-loaded liposomes [36] and polymeric NPs [55]. Multicolor IVM addresses this need well, and multiple strategies have been developed to use intravital fluorescence microscopy to directly and simultaneously visualize transport in the NP, NP degradation, payload release, and even binding of the payload to its therapeutic target.

IVM of drug payload is most straightforward with intrinsically fluorescent therapeutics including anti-neoplastic DNA intercalators such as doxorubicin and daunorubicin [387], mitoxantrone [388], along with tetracycline antibiotics such as doxycycline [389,389], all of which exhibit easily accommodated excitation / emission spectra (λex 450–490 nm, λem 506–650 nm, depending on the drug and its derivatives). Endogenous fluorescence typically exhibits poor brightness and broad excitation and emission spectra, thus requiring high dosing and limiting multicolor imaging. Nonetheless doxorubicin has been repeated used as a model chemotherapeutic for studying intratumoral transport via realtime IVM in tumors [48,390]. In cases that the payload is not fluorescent, chemical conjugations with optimized fluorochromes are required.

Conjugation of small molecule drugs with organic fluorescent dyes represents a highly effective strategy for sensitively monitoring drug transport and imaging molecular drug targets of nanotherapeutics *in vivo*. Over the past decade the list synthesized, validated, and utilized fluorescent-drug conjugates has grown to over a dozen unique compounds, many of which have been successfully employed for IVM applications. Among the most commonly-employed dyes, BODIPYs have been used to label cytotoxic chemotherapeutics including gemcitabine [391], etoposide [392], the microtubule poisons eribulin [56] and docetaxel [54], along with platinum (II) compounds related to carboplatin [154], cisplatin [154,393], and platinum (IV) prodrug derivatives [55]. BODIPY-conjugates of other molecularly targeted therapeutics have been successfully developed, including the kinase inhibitors ibrutinib [156] and foretinib [394]; the poly-ADP-ribose polymerase (PARP) inhibitor olaparib [158,280], and the class-IV antiarrhythmic verapamil [395,396]. Coumarin-conjugated drugs have been effective for *in vitro* analysis [397,398], but their UV excitation and poor brightness generally limits *in vivo* applicability.

Chemical properties of the fluorescent tag, its chemical linker if present, and its conjugation site on the parent compound all have potentially critical impacts on the payload’s performance, much more so than for the actual NP labeling. For instance, labeling vinblastine with BODIPY-FL unexpectedly created a high-affinity pregnane X receptor (PXR) ligand with behavior distinct from either BODIPY-FL or vinblastine parent compounds [399]. In another example, olaparib exhibits prolonged cytoplasmic retention when labeled with the more hydrophobic NIR dye BODIPY-650, as compared to the green emitting BODIPY-FL labeled compound [280]. To overcome similar observations with BODIPY-docetaxel, whereby highly hydrophobic drug does not readily wash-out from cell membranes and thus prevents imaging subcellular drug-target (in this case, tubulin) features, conjugation with the less hydrophobic green-emitting monoalkoxy-BODIPY (MayaFluor) [305] allows imaging of microtubule structures including mitotic spindle formation in live cells [54]. Silicon-rhodamine (SiR) dyes display even more favorable hydrophobic balance, are extremely useful for their compatibility with super-resolution stimulated emission depletion (STED) microscopy, and are NIR-emitting. Moreover, SiR-conjugates efficiently wash-out from cells such that binding to targets such as tubulin [400], actin [400], and the ibrutinib target BTK [157] is exquisitely specific and clear, the last target of which being clearly imaged by IVM in a window chamber model. Nanoencapsulation and prodrug strategies may change the fluorophore-labeling calculus, for instance by favoring hydrophobic BODIPY over more hydrophilic dyes to achieve efficient drug loading and slow drug release. In the case of a nanoencapsulated Pt(IV) prodrug, the BODIPY dye is attached to an aliphatic chain that improves cellular uptake and toxicity and that releases via intracellular Pt reduction to form a reactive dye-free Pt(II) species [55,401].

In contrast to small molecule fluorophore conjugation, nucleic acid and protein delivery often requires a less customized approach to labeling. Numerous strategies exist for protein bioconjugation, including ultra bright bio-orthogonal approaches [402,403], and are reviewed elsewhere [404]. Dye-siRNA labeling kits are commercially available and have been performed for *in vivo* imaging of siRNA-NP delivery [405,406] using Alexa Fluor and cyanine dyes. Nonetheless, fluorescence quenching from RNA complexation has been noted [407], and as with other applications, non-robust fluorophores such as fluorescein have been problematic for intracellular siRNA imaging [408]. Just as with strategies for labeling the NP vehicle itself, NP loading of fluorescent therapeutic payload above a certain density generally leads to self-quenching [308], and so a trade-off exists between optimal imaging of payload within intact NPs versus outside of NPs at much lower concentrations, with the latter benefiting from highest loading. Overall, recent advances in fluorophore conjugation have extended the breadth of tools and strategies available for imaging NP payloads *in vivo,* with increasing appreciation for how physicochemical labeling properties can be optimized for both nanoencapsulation and drug performance outside of the its NP vehicle.

4. Future directions and Challenges

Despite the enormous advances in intravital imaging technology, a number of practical challenges remain particularly with respect to NP imaging. It is perhaps easiest to group these issues by chemical, biological, and technical challenges. The chemical challenges are mostly related to conjugation chemistries, ensuring that fluorochrome modification does not affect the biological behavior, that NPs remain intact and that syntheses are highly reproducible. These issues are often easily surmounted given the growing literature on fluorochrome types, conjugation methods, and their effect on biological behavior.

The biological challenges are still considerable. Tumor-associated macrophages (TAM) and other phagocytic cells are often abundant in the tumor microenvironment and play important roles in the efficacy of different nano preparations. TAM in particular can show considerable plasticity by assuming phenotypes and functions that have different NP uptake patterns and are either tumoricidal (M1-like) or tumor promoting (M2-like). We currently lack a cadre of reporter mice with intact immune systems and where different cell populations express different fluorescent properties. Once established, these could be used to assign functions to these cells with respect to NP behavior. Availability of these models will become all the more critical as nano preparations will invariably be combined with immunotherapy in the future. The ability to temporally and spatially define how different NPs and cells interact with their environment, mediate cellular immunosuppressive or tumoricidal actions, and alter the course of disease progression is required to understand response and resistance mechanisms to nanotherapies, which will ultimately guide next-generation treatments.

Finally, there are a number of technical challenges that have been summarized in other reviews [151]. In essence, it would be ideal to advance orthotopic imaging as opposed to window chamber imaging which is occasionally criticized for its artificiality. Nevertheless, the window chamber is a model system often capable of providing answers not easily obtainable by conventional technologies. Newer fiber-optic approaches and immobilization technologies are being developed to enable true orthotopic imaging without the need for window chambers.

How will we use these emerging new technologies in the future? Box 2 summarizes some of the critical questions that arise with each new therapeutic NP being developed. We argue that IVM represents an invaluable technology to optimize and compare future preparations side-by-side in the same animal. Importantly it is the tool to understand why and when NPs don't work as anticipated. Finally, we expect that IVM technologies will be used more extensively to investigate off-target effects, excretion mechanisms and existing delivery challenges.

Acknowledgments

We thank Jonathan Carlson (MGH) for thoughtful review, and Rainer Kohler (MGH) for images.

Abbreviations

ADME
absorption distribution metabolism excretion

BODIPY
borondipyrromethene

BTK
Bruton's tyrosine kinase

CIW
cranial imaging window

DCE-MRI
dynamic contrast enhanced magnetic resonance imaging

DiO / Dil / DiD / DiR
dialkylcarbocyanine dyes

ECM

extracellular matrix

EGFR
epidermal growth factor receptor

EpCAM
epithelial cell adhesion molecule

EPR
enhanced permeability and retention

FLIM
fluorescence lifetime imaging microscopy

FR
folate receptor

FRET
Förster resonance energy transfer

FUCCI
fluorescence ubiquitination cell cycle indicator

GEMM
genetically engineered mouse model

GFP
green fluorescent protein

HA
hyaluronic acid

HER2
human epidermal growth factor receptor 2

IVM
intravital microscopy

k_{on}/k_{off}
binding and dissociation kinetic rate constants

LeGO
lentiviral gene ontology

M1
inflammatory/tumoricidal phenotype

M2
wound-healing/tumor-promoting phenotype

MPS
mononuclear phagocyte system

MRI
magnetic resonance imaging

NP
nanoparticle

P-gp / MDR1
P-glycoprotein / Multidrug Resistance Gene 1

PAR-1
protease activated receptor 1

PARP
poly ADP ribose polymerase

PD
pharmacodynamics

PEG
poly ethylene glycol

PET/CT
positron emission tomography / computed tomography

PK
pharmacokinetics

PLGA
poly lactic-co-glycolic acid

PRINT
Particle Replication in Non-Wetting Templates

PSMA
prostate specific membrane antigen

Qdot
quantum dot

RFP
red fluorescent protein

RGD
arginine-glycine-aspartic acid

SHG
second harmonic generation

SSTR
somatostatin receptor

SWNT
single-walled carbon nanotube

TAM
tumor associated macrophage

TGFβ
transforming growth factor beta

THG
third harmonic generation

UCNP
up-converting nanoparticle

VEGFR
vascular endothelial growth factor receptor

References

1. Bertrand N, Wu J, Xu X, Kamaly N, Farokhzad OC. Cancer nanotechnology: the impact of passive and active targeting in the era of modern cancer biology. Adv Drug Deliv Rev. 2014; 66:2–25. [PubMed: 24270007]
2. Chow EK, Ho D. Cancer nanomedicine: from drug delivery to imaging. Sci Transl Med. 2013; 5:216rv4.
3. Hrkach J, et al. Preclinical development and clinical translation of a PSMA-targeted docetaxel nanoparticle with a differentiated pharmacological profile. Sci Transl Med. 2012; 4:128ra39.
4. Juliano RL, Stamp D. Pharmacokinetics of liposome-encapsulated anti-tumor drugs. Studies with vinblastine, actinomycin D, cytosine arabinoside, and daunomycin. Biochem Pharmacol. 1978; 27:21–27. [PubMed: 619903]
5. Moghimi SM, Hunter AC, Murray JC. Long-circulating and target-specific nanoparticles: theory to practice. Pharmacol Rev. 2001; 53:283–318. [PubMed: 11356986]
6. O'Brien ME, et al. Reduced cardiotoxicity and comparable efficacy in a phase III trial of pegylated liposomal doxorubicin HCI (CAELYX/Doxil) versus conventional doxorubicin for first-line treatment of metastatic breast cancer. Ann Oncol. 2004; 15:440–449. [PubMed: 14998846]
7. Dhar S, Kolishetti N, Lippard SJ, Farokhzad OC. Targeted delivery of a cisplatin prodrug for safer and more effective prostate cancer therapy in vivo. Proc Natl Acad Sci U S A. 2011; 108:1850–1855. [PubMed: 21233423]
8. Min Y, Caster JM, Eblan MJ, Wang AZ. Clinical Translation of Nanomedicine. Chem Rev. 2015; 115:11147–11190. [PubMed: 26088284]
9. Sheridan C. Proof of concept for next-generation nanoparticle drugs in humans. Nat Biotechnol. 2012; 30:471–473. [PubMed: 22678364]
10. Gradishar WJ, et al. Phase III trial of nanoparticle albumin-bound paclitaxel compared with polyethylated castor oil-based paclitaxel in women with breast cancer. J Clin Oncol. 2005; 23:7794–7803. [PubMed: 16172456]
11. Petersen GH, Alzghari SK, Chee W, Sankari SS, La-Beck NM. Meta-analysis of clinical and preclinical studies comparing the anticancer efficacy of liposomal versus conventional non-liposomal doxorubicin. J Control Release. 2016; S0168–3659:30241–30243.
12. Wilhelm S, et al. Analysis of nanoparticle delivery to tumours. Nat Rev Mat. 2016; 16014:1–12.

13. Valencia PM, et al. Synergistic cytotoxicity of irinotecan and cisplatin in dual-drug targeted polymeric nanoparticles. Nanomedicine (Lond). 2013; 8:687–698. [PubMed: 23075285]
14. Kwong B, Liu H, Irvine DJ. Induction of potent anti-tumor responses while eliminating systemic side effects via liposome-anchored combinatorial immunotherapy. Biomaterials. 2011; 32:5134–5147. [PubMed: 21514665]
15. Cai L, et al. Telodendrimer nanocarrier for co-delivery of paclitaxel and cisplatin: A synergistic combination nanotherapy for ovarian cancer treatment. Biomaterials. 2015; 37:456–468. [PubMed: 25453973]
16. Xu X, et al. Enhancing tumor cell response to chemotherapy through nanoparticle-mediated codelivery of siRNA and cisplatin prodrug. Proc Natl Acad Sci U S A. 2013; 110:18638–18643. [PubMed: 24167294]
17. Johnstone TC, et al. Nanoparticle encapsulation of mitaplatin and the effect thereof on in vivo properties. ACS Nano. 2013; 7:5675–5683. [PubMed: 23697579]
18. Maeda H, Nakamura H, Fang J. The EPR effect for macromolecular drug delivery to solid tumors: Improvement of tumor uptake, lowering of systemic toxicity, and distinct tumor imaging in vivo. Adv Drug Deliv Rev. 2013; 65:71–79. [PubMed: 23088862]
19. Prabhakar U, et al. Challenges and key considerations of the enhanced permeability and retention effect for nanomedicine drug delivery in oncology. Cancer Res. 2013; 73:2412–2417. [PubMed: 23423979]
20. Pattni BS, Chupin VV, Torchilin VP. New Developments in Liposomal Drug Delivery. Chem Rev. 2015:10938–10966. In press. [PubMed: 26010257]
21. Wicki A, Witzigmann D, Balasubramanian V, Huwyler J. Nanomedicine in cancer therapy: challenges, opportunities, and clinical applications. J Control Release. 2015; 200:138–157. [PubMed: 25545217]
22. Caron WP, Song G, Kumar P, Rawal S, Zamboni WC. Interpatient pharmacokinetic and pharmacodynamic variability of carrier-mediated anticancer agents. Clin Pharmacol Ther. 2012; 91:802–812. [PubMed: 22472987]
23. Huo M, et al. Somatostatin receptor-mediated specific delivery of Paclitaxel prodrugs for efficient cancer therapy. J Pharm Sci. 2015; 104:2018–2028. [PubMed: 25820241]
24. Thorek DL, Das S, Grimm J. Molecular imaging using nanoparticle quenchers of Cerenkov luminescence. Small. 2014; 10:3729–3734. [PubMed: 24861843]
25. Vlashi E, Kelderhouse LE, Sturgis JE, Low PS. Effect of folate-targeted nanoparticle size on their rates of penetration into solid tumors. ACS Nano. 2013; 7:8573–8582. [PubMed: 24020507]
26. Kievit FM, et al. Targeting of primary breast cancers and metastases in a transgenic mouse model using rationally designed multifunctional SPIONs. ACS Nano. 2012; 6:2591–2601. [PubMed: 22324543]
27. Bae YH, Park K. Targeted drug delivery to tumors: myths, reality and possibility. J Control Release. 2011; 153:198–205. [PubMed: 21663778]
28. LoRusso P, et al. Abstract CT234: A phase I study of MM-302, a HER2-targeted PEGylated liposomal doxorubicin, in patients with HER2+ metastatic breast cancer. Cancer Research. 2015; 75:CT234.
29. Von Hoff DD, et al. Phase I Study of PSMA-Targeted Docetaxel-Containing Nanoparticle BIND-014 in Patients with Advanced Solid Tumors. Clin Cancer Res. 2016 In press.
30. Matsumoto Y, et al. Vascular bursts enhance permeability of tumour blood vessels and improve nanoparticle delivery. Nat Nanotechnol. 2016 In press.
31. Roode LE, et al. Subtumoral analysis of PRINT nanoparticle distribution reveals targeting variation based on cellular and particle properties. Nanomedicine (Lond). 2016; 12:1053–1062.
32. Liang X, et al. Short-and Long-term Tracking of Anionic Ultra-small Nanoparticles in Kidney. ACS Nano. 2016; 10:387–395. [PubMed: 26743581]
33. Stirland DL, Matsumoto Y, Toh K, Kataoka K, Bae YH. Analyzing spatiotemporal distribution of uniquely fluorescent nanoparticles in xenograft tumors. J Control Release. 2016; 227:38–44. [PubMed: 26873335]
34. Jiang W, Huang Y, An Y, Kim BY. Remodeling Tumor Vasculature to Enhance Delivery of Intermediate-Sized Nanoparticles. ACS Nano. 2015; 9:8689–8696. [PubMed: 26212564]

35. D'Apolito R, et al. Red blood cells affect the margination of microparticles in synthetic microcapillaries and intravital microcirculation as a function of their size and shape. J Control Release. 2015; 217:263–272. [PubMed: 26381900]

36. Rapoport N, Gupta R, Kim YS, O'Neill BE. Polymeric micelles and nanoemulsions as tumor-targeted drug carriers: Insight through intravital imaging. J Control Release. 2015; 206:153–160. [PubMed: 25776738]

37. Dicheva BM, et al. Pharmacokinetics, Tissue Distribution and Therapeutic Effect of Cationic Thermosensitive Liposomal Doxorubicin Upon Mild Hyperthermia. Pharm Res. 2015; 33:627–638. [PubMed: 26518763]

38. Yuan X, et al. Ocular drug delivery nanowafer with enhanced therapeutic efficacy. ACS Nano. 2015; 9:1749–1758. [PubMed: 25585134]

39. Chu D, Gao J, Wang Z. Neutrophil-Mediated Delivery of Therapeutic Nanoparticles across Blood Vessel Barrier for Treatment of Inflammation and Infection. ACS Nano. 2015; 9:11800–11811. [PubMed: 26516654]

40. Liang X, et al. Intravital multiphoton imaging of the selective uptake of water-dispersible quantum dots into sinusoidal liver cells. Small. 2015; 11:1711–1720. [PubMed: 25504510]

41. Cui J, et al. In vivo nanoparticle assessment of pathological endothelium predicts the development of inflow stenosis in murine arteriovenous fistula. ArteriosclerThromb Vasc Biol. 2015; 35:189–196.

42. Fiole D, et al. Two-photon intravital imaging of lungs during anthrax infection reveals long-lasting macrophage-dendritic cell contacts. Infect Immun. 2014; 82:864–872. [PubMed: 24478099]

43. Smith BR, et al. Selective uptake of single-walled carbon nanotubes by circulating monocytes for enhanced tumour delivery. Nat Nanotechnol. 2014; 9:481–487. [PubMed: 24727688]

44. Hak S, et al. Periodicity in tumor vasculature targeting kinetics of ligand-functionalized nanoparticles studied by dynamic contrast enhanced magnetic resonance imaging and intravital microscopy. Angiogenesis. 2014; 17:93–107. [PubMed: 23982332]

45. van de Ven AL, Kim P, Ferrari M, Yun SH. Real-time intravital microscopy of individual nanoparticle dynamics in liver and tumors of live mice. Protoc exch. 2013; doi: 10.1038/protex.2013.049

46. Lee TR, et al. On the near-wall accumulation of injectable particles in the microcirculation: smaller is not better. Sci Rep. 2013; 3:2079. [PubMed: 23801070]

47. Li L, et al. Mild hyperthermia triggered doxorubicin release from optimized stealth thermosensitive liposomes improves intratumoral drug delivery and efficacy. J Control Release. 2013; 168:142–150. [PubMed: 23524188]

48. Seynhaeve AL, Dicheva BM, Hoving S, Koning GA, ten Hagen TL. Intact Doxil is taken up intracellularly and released doxorubicin sequesters in the lysosome: evaluated by in vitro/in vivo live cell imaging. J Control Release. 2013; 172:330–340. [PubMed: 24012486]

49. Shukla S, et al. Increased tumor homing and tissue penetration of the filamentous plant viral nanoparticle Potato virus X. Mol Pharm. 2013; 10:33–42. [PubMed: 22731633]

50. Cabral H, et al. Accumulation of sub-100 nm polymeric micelles in poorly permeable tumours depends on size. Nat Nanotechnol. 2011; 6:815–823. [PubMed: 22020122]

51. Gonda K, Watanabe TM, Ohuchi N, Higuchi H. In vivo nano-imaging of membrane dynamics in metastatic tumor cells using quantum dots. J Biol Chem. 2010; 285:2750–2757. [PubMed: 19917603]

52. Smith BR, Cheng Z, De A, Rosenberg J, Gambhir SS. Dynamic visualization of RGD-quantum dot binding to tumor neovasculature and extravasation in multiple living mouse models using intravital microscopy. Small. 2010; 6:2222–2229. [PubMed: 20862677]

53. Murakami M, et al. Improving drug potency and efficacy by nanocarrier-mediated subcellular targeting. Sci Transl Med. 2011; 3:64ra2.

54. Miller MA, et al. Predicting therapeutic nanomedicine efficacy using a companion magnetic resonance imaging nanoparticle. Sci Transl Med. 2015; 7:314ra183.

55. Miller MA, et al. Tumour-associated macrophages act as a slow-release reservoir of nano-therapeutic Pt(IV) pro-drug. Nat Commun. 2015; 6:8692. [PubMed: 26503691]

56. Laughney AM, et al. Single-cell pharmacokinetic imaging reveals a therapeutic strategy to overcome drug resistance to the microtubule inhibitor eribulin. Sci Transl Med. 2014; 6:261ra152.
57. Orth JD, et al. Analysis of mitosis and antimitotic drug responses in tumors by in vivo microscopy and single-cell pharmacodynamics. Cancer Res. 2011; 71:4608–4616. [PubMed: 21712408]
58. Chittajallu DR, et al. In vivo cell-cycle profiling in xenograft tumors by quantitative intravital microscopy. Nat Methods. 2015; 12:577–585. [PubMed: 25867850]
59. Gabizon A, et al. Prolonged circulation time and enhanced accumulation in malignant exudates of doxorubicin encapsulated in polyethylene-glycol coated liposomes. Cancer Res. 1994; 54:987–992. [PubMed: 8313389]
60. Rodriguez PL, et al. Minimal “Self” peptides that inhibit phagocytic clearance and enhance delivery of nanoparticles. Science. 2013; 339:971–975. [PubMed: 23430657]
61. Zalevsky J, et al. Enhanced antibody half-life improves in vivo activity. Nat Biotechnol. 2010; 28:157–159. [PubMed: 20081867]
62. Kontermann RE. Strategies for extended serum half-life of protein therapeutics. Curr Opin Biotechnol. 2011; 22:868–876. [PubMed: 21862310]
63. Jain RK. Normalization of tumor vasculature: an emerging concept in antiangiogenic therapy. Science. 2005; 307:58–62. [PubMed: 15637262]
64. Harney AS, et al. Real-Time Imaging Reveals Local, Transient Vascular Permeability, and Tumor Cell Intravasation Stimulated by TIE2hi Macrophage-Derived VEGFA. Cancer Discov. 2015; 5:932–943. [PubMed: 26269515]
65. van de Ven AL, et al. Integrated intravital microscopy and mathematical modeling to optimize nanotherapeutics delivery to tumors. AIPAdv. 2012; 2:11208.
66. Juweid M, et al. Micropharmacology of monoclonal antibodies in solid tumors: direct experimental evidence for a binding site barrier. Cancer Res. 1992; 52:5144–5153. [PubMed: 1327501]
67. Choi KY, et al. PEGylation of hyaluronic acid nanoparticles improves tumor targetability in vivo. Biomaterials. 2011; 32:1880–1889. [PubMed: 21159377]
68. Yan F, et al. Molecular imaging-guided photothermal/photodynamic therapy against tumor by iRGD-modified indocyanine green nanoparticles. J Control Release. 2015; 224:217–228. [PubMed: 26739551]
69. Koning GA, et al. Targeting of angiogenic endothelial cells at sites of inflammation by dexamethasone phosphate-containing RGD peptide liposomes inhibits experimental arthritis. Arthritis Rheum. 2006; 54:1198–1208. [PubMed: 16575845]
70. Smith BR, et al. Real-time intravital imaging of RGD-quantum dot binding to luminal endothelium in mouse tumor neovasculature. Nano Lett. 2008; 8:2599–2606. [PubMed: 18386933]
71. Schiffelers RM, et al. Anti-tumor efficacy of tumor vasculature-targeted liposomal doxorubicin. J Control Release. 2003; 91:115–122. [PubMed: 12932643]
72. Smith BR, et al. High-resolution, serial intravital microscopic imaging of nanoparticle delivery and targeting in a small animal tumor model. Nano today. 2013; 8:126–137.
73. Caswell PT, Vadrevu S, Norman JC. Integrins: masters and slaves of endocytic transport. Nat Rev Mol Cell Biol. 2009; 10:843–853. [PubMed: 19904298]
74. Masedunskas A, Porat-Shliom N, Rechache K, Aye MP, Weigert R. Intravital Microscopy Reveals Differences in the Kinetics of Endocytic Pathways between Cell Cultures and Live Animals. Cells. 2012; 1:1121–1132. [PubMed: 24710546]
75. Tada H, Higuchi H, Wanatabe TM, Ohuchi N. In vivo real-time tracking of single quantum dots conjugated with monoclonal anti-HER2 antibody in tumors of mice. Cancer Res. 2007; 67:1138–1144. [PubMed: 17283148]
76. Kikushima K, Kita S, Higuchi H. A non-invasive imaging for the in vivo tracking of high-speed vesicle transport in mouse neutrophils. Sci Rep. 2013; 3:1913. [PubMed: 23722417]
77. Jones SW, et al. Nanoparticle clearance is governed by Th1/Th2 immunity and strain background. J Clin Invest. 2013; 123:3061–3073. [PubMed: 23778144]
78. Kai MP, et al. Tumor Presence Induces Global Immune Changes and Enhances Nanoparticle Clearance. ACS Nano. 2015; 10:861–870. [PubMed: 26592524]

79. Komohara Y, Fujiwara Y, Ohnishi K, Takeya M. Tumor-associated macrophages: Potential therapeutic targets for anti-cancer therapy. Adv Drug Deliv Rev. 2016; 99:180–185. [PubMed: 26621196]

80. Allison AG, Gregoriadis G. Liposomes as immunological adjuvants. Nature. 1974; 252:252.

81. van Rooijen N, van Nieuwmegen R. Liposomes in immunology: the immune response against antigen-containing liposomes. Immunol Commun. 1977; 6:489–498. [PubMed: 924513]

82. Alving CR, et al. Therapy of leishmaniasis: superior efficacies of liposome-encapsulated drugs. Proc Natl Acad Sci U S A. 1978; 75:2959–2963. [PubMed: 208079]

83. Alving CR. Delivery of liposome-encapsulated drugs to macrophages. Pharmacol Ther. 1983; 22:407–424. [PubMed: 6361805]

84. Fenaroli F, et al. Nanoparticles as drug delivery system against tuberculosis in zebrafish embryos: direct visualization and treatment. ACS Nano. 2014; 8:7014–7026. [PubMed: 24945994]

85. Lim WS, et al. Leukemia-selective uptake and cytotoxicity of CPX-351, a synergistic fixed-ratio cytarabine:daunorubicin formulation, in bone marrow xenografts. Leuk Res. 2010; 34:1214–1223. [PubMed: 20138667]

86. Mitchell MJ, Chen CS, Ponmudi V, Hughes AD, King MR. E-selectin liposomal and nanotube-targeted delivery of doxorubicin to circulating tumor cells. J Control Release. 2012; 160:609–617. [PubMed: 22421423]

87. Leimgruber A, et al. Behavior of endogenous tumor-associated macrophages assessed in vivo using a functionalized nanoparticle. Neoplasia. 2009; 11:459–468. [PubMed: 19412430]

88. Bagalkot V, et al. Hybrid nanoparticles improve targeting to inflammatory macrophages through phagocytic signals. J Control Release. 2015; 217:243–255. [PubMed: 26386437]

89. Pande AN, Kohler RH, Aikawa E, Weissleder R, Jaffer FA. Detection of macrophage activity in atherosclerosis in vivo using multichannel, high-resolution laser scanning fluorescence microscopy. J Biomed Opt. 2006; 11:021009. [PubMed: 16674184]

90. Wang Z, Li J, Cho J, Malik AB. Prevention of vascular inflammation by nanoparticle targeting of adherent neutrophils. Nat Nanotechnol. 2014; 9:204–210. [PubMed: 24561355]

91. Manolova V, et al. Nanoparticles target distinct dendritic cell populations according to their size. Eur J Immunol. 2008; 38:1404–1413. [PubMed: 18389478]

92. Zhao Y, et al. Near-infrared fluorescence energy transfer imaging of nanoparticle accumulation and dissociation kinetics in tumor-bearing mice. ACS Nano. 2013; 7:10362–10370. [PubMed: 24134041]

93. Zou P, Chen H, Paholak HJ, Sun D. Noninvasive fluorescence resonance energy transfer imaging of in vivo premature drug release from polymeric nanoparticles. Mol Pharm. 2013; 10:4185–4194. [PubMed: 24033270]

94. Prise KM, O'Sullivan JM. Radiation-induced bystander signalling in cancer therapy. Nat Rev Cancer. 2009; 9:351–360. [PubMed: 19377507]

95. Alexandre J, Hu Y, Lu W, Pelicano H, Huang P. Novel action of paclitaxel against cancer cells: bystander effect mediated by reactive oxygen species. Cancer Res. 2007; 67:3512–3517. [PubMed: 17440056]

96. Blair BG, Larson CA, Safaei R, Howell SB. Copper transporter 2 regulates the cellular accumulation and cytotoxicity of Cisplatin and Carboplatin. Clin Cancer Res. 2009; 15:4312–4321. [PubMed: 19509135]

97. Safaei R. Role of copper transporters in the uptake and efflux of platinum containing drugs. Cancer Lett. 2006; 234:34–39. [PubMed: 16297532]

98. Sun T, Guan X, Zheng M, Jing X, Xie Z. Mitochondria-Localized Fluorescent BODIPY-Platinum Conjugate. ACS Med Chem Lett. 2015; 6:430–433. [PubMed: 25941554]

99. Pusztai L, et al. Phase II study of tariquidar, a selective P-glycoprotein inhibitor, in patients with chemotherapy-resistant, advanced breast carcinoma. Cancer. 2005; 104:682–691. [PubMed: 15986399]

100. Patil Y, Sadhukha T, Ma L, Panyam J. Nanoparticle-mediated simultaneous and targeted delivery of paclitaxel and tariquidar overcomes tumor drug resistance. J Control Release. 2009; 136:21–29. [PubMed: 19331851]

101. Davies D. Understanding biofilm resistance to antibacterial agents. Nat Rev Drug Discov. 2003; 2:114–122. [PubMed: 12563302]
102. Miao L, Lin CM, Huang L. Stromal barriers and strategies for the delivery of nanomedicine to desmoplastic tumors. J Control Release. 2015; 219:192–204. [PubMed: 26277065]
103. Pridgen EM, et al. Transepithelial transport of Fc-targeted nanoparticles by the neonatal fc receptor for oral delivery. Sci Transl Med. 2013; 5:213ra167.
104. Ross KA, et al. Nano-enabled delivery of diverse payloads across complex biological barriers. J Control Release. 2015; 219:548–559. [PubMed: 26315817]
105. Ensign LM, et al. Mucus-penetrating nanoparticles for vaginal drug delivery protect against herpes simplex virus. Sci Transl Med. 2012; 4:138ra79.
106. Li X, et al. Control of nanoparticle penetration into biofilms through surface design. Chem Commun (Camb). 2015; 51:282–285. [PubMed: 25407407]
107. Forier K, et al. Transport of nanoparticles in cystic fibrosis sputum and bacterial biofilms by single-particle tracking microscopy. Nanomedicine (Lond). 2013; 8:935–949. [PubMed: 23035662]
108. Lieleg O, Baumgärtel RM, Bausch AR. Selective filtering of particles by the extracellular matrix: an electrostatic bandpass. Biophys J. 2009; 97:1569–1577. [PubMed: 19751661]
109. Alexander S, Weigelin B, Winkler F, Friedl P. Preclinical intravital microscopy of the tumour-stroma interface: invasion, metastasis, and therapy response. Curr Opin Cell Biol. 2013; 25:659–671. [PubMed: 23896198]
110. Yokoi K, et al. Capillary-wall collagen as a biophysical marker of nanotherapeutic permeability into the tumor microenvironment. Cancer Res. 2014; 74:4239–4246. [PubMed: 24853545]
111. Wong C, et al. Multistage nanoparticle delivery system for deep penetration into tumor tissue. Proc Natl Acad Sci U S A. 2011; 108:2426–2431. [PubMed: 21245339]
112. Provenzano PP, et al. Enzymatic targeting of the stroma ablates physical barriers to treatment of pancreatic ductal adenocarcinoma. Cancer Cell. 2012; 21:418–429. [PubMed: 22439937]
113. Liu J, et al. TGF-β blockade improves the distribution and efficacy of therapeutics in breast carcinoma by normalizing the tumor stroma. Proc Natl Acad Sci U S A. 2012; 109:16618–16623. [PubMed: 22996328]
114. Roediger B, et al. Cutaneous immunosurveillance and regulation of inflammation by group 2 innate lymphoid cells. Nat Immunol. 2013; 14:564–573. [PubMed: 23603794]
115. Wang HW, Langohr IM, Sturek M, Cheng JX. Imaging and quantitative analysis of atherosclerotic lesions by CARS-based multimodal nonlinear optical microscopy. Arterioscler Thromb Vasc Biol. 2009; 29:1342–1348. [PubMed: 19520975]
116. Saxena A, et al. High-resolution optical mapping of inflammatory macrophages following endovascular arterial injury. Mol Imaging Biol. 2013; 15:282–289. [PubMed: 23090852]
117. Elsaesser A, Howard CV. Toxicology of nanoparticles. Adv Drug Deliv Rev. 2012; 64:129–137. [PubMed: 21925220]
118. Lin CJ, Kang N, Lee JY, Lee HS, Dong CY. Visualizing and quantifying difference in cytoplasmic and nuclear metabolism in the hepatobiliary system in vivo. J Biomed Opt. 2015; 20:016020. [PubMed: 25611866]
119. Sandoval RM, Kennedy MD, Low PS, Molitoris BA. Uptake and trafficking of fluorescent conjugates of folic acid in intact kidney determined using intravital two-photon microscopy. Am J Physiol Cell Physiol. 2004; 287:C517–26. [PubMed: 15102609]
120. Liu X, Thorling CA, Jin L, Roberts MS. Intravital multiphoton imaging of rhodamine 123 in the rat liver after intravenous dosing. IntraVital. 2012; 1:54–59.
121. Weiss M, Liu X, Thorling CA, Roberts MS. Functional characterization of hepatic transporters using intravital microscopy. Eur J Pharm Sci. 2013; 49:845–849. [PubMed: 23791640]
122. Calcagno AM, Kim IW, Wu CP, Shukla S, Ambudkar SV. ABC drug transporters as molecular targets for the prevention of multidrug resistance and drug-drug interactions. Curr Drug Deliv. 2007; 4:324–333. [PubMed: 17979652]
123. Chavanpatil MD, et al. Surfactant-polymer nanoparticles overcome P-glycoprotein-mediated drug efflux. Mol Pharm. 2007; 4:730–738. [PubMed: 17705442]

124. Zhang Y, et al. Effect of poly(ethylene glycol)-block-polylactide nanoparticles on hepatic cells of mouse: low cytotoxicity, but efflux of the nanoparticles by ATP-binding cassette transporters. Eur J Pharm Biopharm. 2007; 66:268–280. [PubMed: 17182234]
125. Laemmel E, et al. Fibered confocal fluorescence microscopy (Cell-viZio) facilitates extended imaging in the field of microcirculation. A comparison with intravital microscopy. J Vasc Res. 2004; 41:400–411. [PubMed: 15467299]
126. König K. Clinical multiphoton tomography. J Biophotonics. 2008; 1:13–23. [PubMed: 19343631]
127. Degueldre M, Vandromme J, de Wind A, Feoli F. Real-time in-vivo microscopic imaging of the cervix using confocal laser endomicroscopy: preliminary observations and feasibility study. Eur J Cancer Prev. 2015
128. Wellikoff AS, et al. Comparison of in vivo probe-based confocal laser endomicroscopy with histopathology in lung cancer: A move toward optical biopsy. Respirology. 2015; 20:967–974. [PubMed: 26094505]
129. Kuiper T, van den Broek FJ, van Eeden S, Fockens P, Dekker E. Feasibility and accuracy of confocal endomicroscopy in comparison with narrow-band imaging and chromoendoscopy for the differentiation of colorectal lesions. Am J Gastroenterol. 2012; 107:543–550. [PubMed: 22433922]
130. Sanai N, et al. Intraoperative confocal microscopy in the visualization of 5-aminolevulinic acid fluorescence in low-grade gliomas. J Neurosurg. 2011; 115:740–748. [PubMed: 21761971]
131. van den Berg NS, van Leeuwen FW, van der Poel HG. Fluorescence guidance in urologic surgery. Curr Opin Urol. 2012; 22:109–120. [PubMed: 22262249]
132. Neuman BP, et al. Real-time, near-infrared fluorescence imaging with an optimized dye/light source/camera combination for surgical guidance of prostate cancer. Clin Cancer Res. 2015; 21:771–780. [PubMed: 25501577]
133. Whitley MJ, et al. A mouse-human phase 1 co-clinical trial of a protease-activated fluorescent probe for imaging cancer. Sci Transl Med. 2016; 8:320ra4.
134. Fisher DT, et al. Intraoperative intravital microscopy permits the study of human tumour vessels. Nat Commun. 2016; 7:10684. [PubMed: 26883450]
135. Dósa E, et al. MRI using ferumoxytol improves the visualization of central nervous system vascular malformations. Stroke. 2011; 42:1581–1588. [PubMed: 21493906]
136. Gaglia JL, et al. Noninvasive mapping of pancreatic inflammation in recent-onset type-1 diabetes patients. Proc Natl Acad Sci U S A. 2015; 112:2139–2144. [PubMed: 25650428]
137. Harisinghani MG, et al. Noninvasive detection of clinically occult lymph-node metastases in prostate cancer. N Engl J Med. 2003; 348:2491–2499. [PubMed: 12815134]
138. Harisinghani M, Ross RW, Guimaraes AR, Weissleder R. Utility of a new bolus-injectable nanoparticle for clinical cancer staging. Neoplasia. 2007; 9:1160–1165. [PubMed: 18084623]
139. Thorek DL, et al. Non-invasive mapping of deep-tissue lymph nodes in live animals using a multimodal PET/MRI nanoparticle. Nat Commun. 2014; 5:3097. [PubMed: 24445347]
140. Miller K, et al. Effect of pre-treatment with cyclophosphamide on MM-302 (HER2-targeted liposomal doxorubicin) deposition in HER2-positive metastatic breast cancer patients assessed by 64Cu-MM-302 PET/CT. Cancer Res. 2015; 75:P4–15.
141. Phillips E, et al. Clinical translation of an ultrasmall inorganic optical-PET imaging nanoparticle probe. Sci Transl Med. 2014; 6:260ra149.
142. Day ES, et al. Vascular-targeted photothermal therapy of an orthotopic murine glioma model. Nanomedicine (Lond). 2012; 7:1133–1148. [PubMed: 22583571]
143. Read TA, et al. Intravital microscopy reveals novel antivascular and antitumor effects of endostatin delivered locally by alginate-encapsulated cells. Cancer Res. 2001; 61:6830–6837. [PubMed: 11559558]
144. Li JL, et al. Intravital multiphoton imaging of immune responses in the mouse ear skin. Nat Protoc. 2012; 7:221–234. [PubMed: 22240584]
145. Ritsma L, et al. Surgical implantation of an abdominal imaging window for intravital microscopy. Nat Protoc. 2013; 8:583–594. [PubMed: 23429719]

146. Ritsma L, et al. Intravital microscopy through an abdominal imaging window reveals a pre-micrometastasis stage during liver metastasis. Sci Transl Med. 2012; 4:158ra145.
147. Kedrin D, et al. Intravital imaging of metastatic behavior through a mammary imaging window. Nat Methods. 2008; 5:1019–1021. [PubMed: 18997781]
148. Jain RK, Munn LL, Fukumura D. Measuring vascular permeability in mice. Cold Spring Harb Protoc. 2013; 2013:444–446. [PubMed: 23637370]
149. Textor J, et al. Defining the quantitative limits of intravital two-photon lymphocyte tracking. Proc Natl Acad Sci U S A. 2011; 108:12401–12406. [PubMed: 21734152]
150. Geva-Zatorsky N, et al. In vivo imaging and tracking of host-microbiota interactions via metabolic labeling of gut anaerobic bacteria. Nat Med. 2015; 21:1091–1100. [PubMed: 26280120]
151. Pittet MJ, Weissleder R. Intravital imaging. Cell. 2011; 147:983–991. [PubMed: 22118457]
152. Condeelis J, Weissleder R. In vivo imaging in cancer. Cold Spring Harb Perspect Biol. 2010; 2:a003848. [PubMed: 20861158]
153. Alieva M, Ritsma L, Giedt RJ, Weissleder… R. Imaging windows for long-term intravital imaging: General overview and technical insights. IntraVital. 2014; 3:e29917. [PubMed: 28243510]
154. Miller MA, Askevold B, Yang KS, Kohler RH, Weissleder R. Platinum compounds for high-resolution in vivo cancer imaging. Chem Med Chem. 2014; 9:1131–1135. [PubMed: 24504646]
155. Nuhn L, et al. Aggregation behavior of cationic nanohydrogel particles in human blood serum. Biomacromolecules. 2014; 15:1526–1533. [PubMed: 24697603]
156. Turetsky A, Kim E, Kohler RH, Miller MA, Weissleder R. Single cell imaging of Bruton's tyrosine kinase using an irreversible inhibitor. Sci Rep. 2014; 4:4782. [PubMed: 24759210]
157. Kim E, et al. Optimized Near-IR fluorescent agents for in vivo imaging of Btk expression. Bioconjug Chem. 2015; 26:1513–1518. [PubMed: 26017814]
158. Thurber GM, et al. Single-cell and subcellular pharmacokinetic imaging allows insight into drug action in vivo. Nat Commun. 2013; 4:1504. [PubMed: 23422672]
159. He W, Wang H, Hartmann LC, Cheng JX, Low PS. In vivo quantitation of rare circulating tumor cells by multiphoton intravital flow cytometry. Proc Natl Acad Sci U S A. 2007; 104:11760–11765. [PubMed: 17601776]
160. Reiner T, et al. Accurate measurement of pancreatic islet beta-cell mass using a second-generation fluorescent exendin-4 analog. Proc Natl Acad Sci U S A. 2011; 108:12815–12820. [PubMed: 21768367]
161. Thurber GM, Weissleder R. Quantitating antibody uptake in vivo: conditional dependence on antigen expression levels. Mol Imaging Biol. 2011; 13:623–632. [PubMed: 20809210]
162. Metildi CA, et al. In vivo fluorescence imaging of gastrointestinal stromal tumors using fluorophore-conjugated anti-KIT antibody. Ann Surg Oncol. 2013; 20(Suppl 3):S693–700. [PubMed: 23943029]
163. Koga S, et al. In vivo subcellular imaging of tumors in mouse models using a fluorophore-conjugated anti-carcinoembryonic antigen antibody in two-photon excitation microscopy. Cancer Sci. 2014; 105:1299–1306. [PubMed: 25117702]
164. McElroy M, et al. Imaging of primary and metastatic pancreatic cancer using a fluorophore-conjugated anti-CA19-9 antibody for surgical navigation. World J Surg. 2008; 32:1057–1066. [PubMed: 18264829]
165. Arwert E, et al. Visualizing the dynamics of EGFR activity and antiglioma therapies in vivo. Cancer Res. 2007; 67:7335–7342. [PubMed: 17671203]
166. Steven P, Bock F, Hüttmann G, Cursiefen C. Intravital two-photon microscopy of immune cell dynamics in corneal lymphatic vessels. PLoS One. 2011; 6:e26253. [PubMed: 22028842]
167. Chiang EY, Hidalgo A, Chang J, Frenette PS. Imaging receptor microdomains on leukocyte subsets in live mice. Nat Methods. 2007; 4:219–222. [PubMed: 17322889]
168. Falati S, Gross P, Merrill-Skoloff G, Furie BC, Furie B. Real-time in vivo imaging of platelets, tissue factor and fibrin during arterial thrombus formation in the mouse. Nat Med. 2002; 8:1175–1181. [PubMed: 12244306]

169. Dubach JM, et al. In vivo imaging of specific drug-target binding at subcellular resolution. Nat Commun. 2014; 5:3946. [PubMed: 24867710]
170. Shah K, Jacobs A, Breakefield XO, Weissleder R. Molecular imaging of gene therapy for cancer. Gene Ther. 2004; 11:1175–1187. [PubMed: 15141158]
171. Medarova Z, Pham W, Farrar C, Petkova V, Moore A. In vivo imaging of siRNA delivery and silencing in tumors. Nat Med. 2007; 13:372–377. [PubMed: 17322898]
172. Yin H, et al. Therapeutic genome editing by combined viral and non-viral delivery of CRISPR system components in vivo. Nat Biotechnol. 2016; 34:328–333. [PubMed: 26829318]
173. Hickerson RP, et al. Non-Invasive Intravital Imaging of siRNA-Mediated Mutant Keratin Gene Repression in Skin. Mol Imaging Bio. 2015; 18:34–42.
174. Leuschner F, et al. Silencing of CCR2 in myocarditis. Eur Heart J. 2015; 36:1478–1488. [PubMed: 24950695]
175. Kortylewski M, et al. In vivo delivery of siRNA to immune cells by conjugation to a TLR9 agonist enhances antitumor immune responses. Nat Biotechnol. 2009; 27:925–932. [PubMed: 19749770]
176. Sakaue-Sawano A, et al. Visualizing spatiotemporal dynamics of multicellular cell-cycle progression. Cell. 2008; 132:487–498. [PubMed: 18267078]
177. Yang KS, Kohler RH, Landon M, Giedt R, Weissleder R. Single cell resolution in vivo imaging of DNA damage following PARP inhibition. Sci Rep. 2015; 5:10129. [PubMed: 25984718]
178. Earley S, et al. In vivo imaging of drug-induced mitochondrial outer membrane permeabilization at single-cell resolution. Cancer Res. 2012; 72:2949–2956. [PubMed: 22505651]
179. Cao L, Kobayakawa S, Yoshiki A, Abe K. High resolution intravital imaging of subcellular structures of mouse abdominal organs using a microstage device. PLoS One. 2012; 7:e33876. [PubMed: 22479464]
180. Karanam K, Kafri R, Loewer A, Lahav G. Quantitative live cell imaging reveals a gradual shift between DNA repair mechanisms and a maximal use of HR in mid S phase. Mol Cell. 2012; 47:320–329. [PubMed: 22841003]
181. Lahav G, et al. Dynamics of the p53-Mdm2 feedback loop in individual cells. Nat Genet. 2004; 36:147–150. [PubMed: 14730303]
182. Ashton S, et al. Aurora kinase inhibitor nanoparticles target tumors with favorable therapeutic index in vivo. Sci Transl Med. 2016; 8:325ra17.
183. Nobis M, et al. Intravital FLIM-FRET imaging reveals dasatinib-induced spatial control of src in pancreatic cancer. Cancer Res. 2013; 73:4674–4686. [PubMed: 23749641]
184. Hirata E, et al. Intravital imaging reveals how BRAF inhibition generates drug-tolerant microenvironments with high integrin (β1/FAK signaling. Cancer Cell. 2015; 27:574–588. [PubMed: 25873177]
185. Kumagai Y, et al. Heterogeneity in ERK activity as visualized by in vivo FRET imaging of mammary tumor cells developed in MMTV-Neu mice. Oncogene. 2015; 34:1051–1057. [PubMed: 24632612]
186. Komatsu N, et al. Development of an optimized backbone of FRET biosensors for kinases and GTPases. Mol Biol Cell. 2011; 22:4647–4656. [PubMed: 21976697]
187. Fritz RD, et al. A versatile toolkit to produce sensitive FRET biosensors to visualize signaling in time and space. Sci Signal. 2013; 6:rs12. [PubMed: 23882122]
188. Johnson SA, You Z, Hunter T. Monitoring ATM kinase activity in living cells. DNA Repair (Amst). 2007; 6:1277–1284. [PubMed: 17428747]
189. Regot S, Hughey JJ, Bajar BT, Carrasco S, Covert MW. High-sensitivity measurements of multiple kinase activities in live single cells. Cell. 2014; 157:1724–1734. [PubMed: 24949979]
190. Gross SM, Rotwein P. Akt signaling dynamics in individual cells. J Cell Sci. 2015; 128:2509–2519. [PubMed: 26040286]
191. Oudin MJ, et al. Tumor cell-driven extracellular matrix remodeling enables haptotaxis during metastatic progression. Cancer Discov. 2016; 6:516–531. [PubMed: 26811325]

192. Hirata E, et al. In vivo fluorescence resonance energy transfer imaging reveals differential activation of Rho-family GTPases in glioblastoma cell invasion. J Cell Sci. 2012; 125:858–868. [PubMed: 22399802]
193. Kagawa Y, et al. Cell cycle-dependent Rho GTPase activity dynamically regulates cancer cell motility and invasion in vivo. PLoS One. 2013; 8:e83629. [PubMed: 24386239]
194. Ouyang M, et al. Simultaneous visualization of protumorigenic Src and MT1-MMP activities with fluorescence resonance energy transfer. Cancer Res. 2010; 70:2204–2212. [PubMed: 20197470]
195. Chapnick DA, Bunker E, Liu X. A biosensor for the activity of the “sheddase” TACE (ADAM17) reveals novel and cell type-specific mechanisms of TACE activation. Sci Signal. 2015; 8:rs1. [PubMed: 25714465]
196. Miller MA, et al. Reduced Proteolytic Shedding of Receptor Tyrosine Kinases Is a Post-Translational Mechanism of Kinase Inhibitor Resistance. Cancer Discov. 2016; 6:382–399. [PubMed: 26984351]
197. Miller MA, et al. ADAM-10 and -17 regulate endometriotic cell migration via concerted ligand and receptor shedding feedback on kinase signaling. Proc Natl Acad Sci U S A. 2013; 110:E2074–83. [PubMed: 23674691]
198. Mandl JN, et al. Quantification of lymph node transit times reveals differences in antigen surveillance strategies of naive CD4+ and CD8+ T cells. Proc Natl Acad Sci U S A. 2012; 109:18036–18041. [PubMed: 23071319]
199. Clatworthy MR, et al. Immune complexes stimulate CCR7-dependent dendritic cell migration to lymph nodes. Nat Med. 2014; 20:1458–1463. [PubMed: 25384086]
200. Germain RN, Robey EA, Cahalan MD. A decade of imaging cellular motility and interaction dynamics in the immune system. Science. 2012; 336:1676–1681. [PubMed: 22745423]
201. Livet J, et al. Transgenic strategies for combinatorial expression of fluorescent proteins in the nervous system. Nature. 2007; 450:56–62. [PubMed: 17972876]
202. Pucci F, et al. SCS macrophages suppress melanoma by restricting tumor-derived vesicle-B cell interactions. Science. 2016; 352:242–246. [PubMed: 26989197]
203. Zomer A, et al. In Vivo imaging reveals extracellular vesicle-mediated phenocopying of metastatic behavior. Cell. 2015; 161:1046–1057. [PubMed: 26000481]
204. Pittet MJ, Swirski FK, Reynolds F, Josephson L, Weissleder R. Labeling of immune cells for in vivo imaging using magnetofluorescent nanoparticles. Nat Protoc. 2006; 1:73–79. [PubMed: 17406214]
205. Weissleder R, Nahrendorf M, Pittet MJ. Imaging macrophages with nanoparticles. Nat Mater. 2014; 13:125–138. [PubMed: 24452356]
206. Parak WJ, Pellegrino T, Plank C. Labelling of cells with quantum dots. Nanotechnology. 2005; 16:R9–R25. [PubMed: 21727419]
207. Wu TJ, et al. Tracking the engraftment and regenerative capabilities of transplanted lung stem cells using fluorescent nanodiamonds. Nat Nanotechnol. 2013; 8:682–689. [PubMed: 23912062]
208. Yang H, et al. One-step generation of mice carrying reporter and conditional alleles by CRISPR/Cas-mediated genome engineering. Cell. 2013; 154:1370–1379. [PubMed: 23992847]
209. Cai D, Cohen KB, Luo T, Lichtman JW, Sanes JR. Improved tools for the Brainbow toolbox. Nat Methods. 2013; 10:540–547.
210. Weber K, Bartsch U, Stocking C, Fehse B. A multicolor panel of novel lentiviral “gene ontology” (LeGO) vectors for functional gene analysis. Mol Ther. 2008; 16:698–706. [PubMed: 18362927]
211. Michaelis M, Selt F, Rothweiler F, Wiese M, Cinatl J. ABCG2 impairs the activity of the aurora kinase inhibitor tozasertib but not of alisertib. BMC Res Notes. 2015; 8:484. [PubMed: 26415506]
212. Coffey SE, Giedt RJ, Weissleder R. Automated analysis of clonal cancer cells by intravital imaging. Intravital. 2013; 2:e26138.
213. Wu JW, et al. Defining Clonal Color in Fluorescent Multi-Clonal Tracking. Sci Rep. 2016; 6:24303. [PubMed: 27073117]

214. Malide D, Métais JY, Dunbar CE. Dynamic clonal analysis of murine hematopoietic stem and progenitor cells marked by 5 fluorescent proteins using confocal and multiphoton microscopy. Blood. 2012; 120:e105–16. [PubMed: 22995900]

215. Tas JM, et al. Visualizing antibody affinity maturation in germinal centers. Science. 2016; 351:1048–1054. [PubMed: 26912368]

216. Tomura M, et al. Monitoring cellular movement in vivo with photoconvertible fluorescence protein “Kaede” transgenic mice. Proc Natl Acad Sci U S A. 2008; 105:10871–10876. [PubMed: 18663225]

217. Carlson AL, et al. Tracking single cells in live animals using a photoconvertible near-infrared cell membrane label. PLoS One. 2013; 8:e69257. [PubMed: 23990881]

218. Müller AJ, et al. Photoconvertible pathogen labeling reveals nitric oxide control of Leishmania major infection in vivo via dampening of parasite metabolism. Cell Host Microbe. 2013; 14:460–467. [PubMed: 24139402]

219. Yuan F, et al. Vascular permeability in a human tumor xenograft: molecular size dependence and cutoff size. Cancer Res. 1995; 55:3752–3756. [PubMed: 7641188]

220. Jain RK, Munn LL, Fukumura D. Dissecting tumour pathophysiology using intravital microscopy. Nat Rev Cancer. 2002; 2:266–276. [PubMed: 12001988]

221. Yuan F, et al. Microvascular permeability and interstitial penetration of sterically stabilized (stealth) liposomes in a human tumor xenograft. Cancer Res. 1994; 54:3352–3356. [PubMed: 8012948]

222. Zoumi A, Yeh A, Tromberg BJ. Imaging cells and extracellular matrix in vivo by using second-harmonic generation and two-photon excited fluorescence. Proc Natl Acad Sci U S A. 2002; 99:11014–11019. [PubMed: 12177437]

223. Huang SH, et al. Imaging of zebrafish in vivo with second-harmonic generation reveals shortened sarcomeres associated with myopathy induced by statin. PLoS One. 2011; 6:e24764. [PubMed: 21966365]

224. Farrar MJ, Wise FW, Fetcho JR, Schaffer CB. In vivo imaging of myelin in the vertebrate central nervous system using third harmonic generation microscopy. Biophys J. 2011; 100:1362–1371. [PubMed: 21354410]

225. Rehberg M, Krombach F, Pohl U, Dietzel S. Label-free 3D visualization of cellular and tissue structures in intact muscle with second and third harmonic generation microscopy. PLoS One. 2011; 6:e28237. [PubMed: 22140560]

226. Dickson PV, et al. Bevacizumab-induced transient remodeling of the vasculature in neuroblastoma xenografts results in improved delivery and efficacy of systemically administered chemotherapy. Clin Cancer Res. 2007; 13:3942–3950. [PubMed: 17606728]

227. Yuan H, et al. Effects of fractionated radiation on the brain vasculature in a murine model: blood-brain barrier permeability, astrocyte proliferation, and ultrastructural changes. Int J Radiat Oncol Biol Phys. 2006; 66:860–866. [PubMed: 17011458]

228. Stieger SM, et al. Enhancement of vascular permeability with low-frequency contrast-enhanced ultrasound in the chorioallantoic membrane model. Radiology. 2007; 243:112–121. [PubMed: 17392250]

229. Li L, et al. Triggered content release from optimized stealth thermosensitive liposomes using mild hyperthermia. J Control Release. 2010; 143:274–279. [PubMed: 20074595]

230. Bagley AF, et al. Endothelial Thermotolerance Impairs Nanoparticle Transport in Tumors. Cancer Res. 2015; 75:3255–3267. [PubMed: 26122846]

231. Smith BR, et al. Shape matters: intravital microscopy reveals surprising geometrical dependence for nanoparticles in tumor models of extravasation. Nano Lett. 2012; 12:3369–3377. [PubMed: 22650417]

232. Egawa G, et al. Intravital analysis of vascular permeability in mice using two-photon microscopy. Sci Rep. 2013; 3:1932. [PubMed: 23732999]

233. Haep L, et al. Interferon Gamma Counteracts the Angiogenic Switch and Induces Vascular Permeability in Dextran Sulfate Sodium Colitis in Mice. Inflamm Bowel Dis. 2015; 21:2360–2371. [PubMed: 26164664]

234. Cheng KC, Xin X, Clark DP, La Riviere P. Whole-animal imaging, gene function, and the Zebrafish Phenome Project. Curr Opin Genet Dev. 2011; 21:620–629. [PubMed: 21963132]
235. Höckendorf B, Thumberger T, Wittbrodt J. Quantitative analysis of embryogenesis: a perspective for light sheet microscopy. Dev Cell. 2012; 23:1111–1120. [PubMed: 23237945]
236. Keller PJ. Imaging morphogenesis: technological advances and biological insights. Science. 2013; 340:1234168. [PubMed: 23744952]
237. O'Reilly LP, Luke CJ, Perlmutter DH, Silverman GA, Pak SC. C. elegans in high-throughput drug discovery. Adv Drug Deliv Rev. 2014; 69–70:247–253.
238. Schmitt SM, Gull M, Brändli AW. Engineering Xenopus embryos for phenotypic drug discovery screening. Adv Drug Deliv Rev. 2014; 69–70:225–246.
239. Fako VE, Furgeson DY. Zebrafish as a correlative and predictive model for assessing biomaterial nanotoxicity. Adv Drug Deliv Rev. 2009; 61:478–486. [PubMed: 19389433]
240. Rozenberg GI, Monahan KB, Torrice C, Bear JE, Sharpless NE. Metastasis in an orthotopic murine model of melanoma is independent of RAS/RAF mutation. Melanoma Res. 2010; 20:361–371. [PubMed: 20679910]
241. Ritsma L, et al. Intestinal crypt homeostasis revealed at single-stem-cell level by in vivo live imaging. Nature. 2014; 507:362–365. [PubMed: 24531760]
242. Bochner F, Fellus-Alyagor L, Kalchenko V, Shinar S, Neeman M. A Novel Intravital Imaging Window for Longitudinal Microscopy of the Mouse Ovary. Sci Rep. 2015; 5:12446. [PubMed: 26207832]
243. Xu HT, Pan F, Yang G, Gan WB. Choice of cranial window type for in vivo imaging affects dendritic spine turnover in the cortex. Nat Neurosci. 2007; 10:549–551. [PubMed: 17417634]
244. Flusberg BA, et al. High-speed, miniaturized fluorescence microscopy in freely moving mice. Nat Methods. 2008; 5:935–938. [PubMed: 18836457]
245. Vinegoni C, Lee S, Aguirre AD, Weissleder R. New techniques for motion-artifact-free in vivo cardiac microscopy. Front Physiol. 2015; 6:147. [PubMed: 26029116]
246. Vinegoni C, et al. Advances in measuring single-cell pharmacology in vivo. Drug Discov Today. 2015; 20:1087–1092. [PubMed: 26024776]
247. Aguirre AD, Vinegoni C, Sebas M, Weissleder R. Intravital imaging of cardiac function at the single-cell level. Proc Natl Acad Sci U S A. 2014; 111:11257–11262. [PubMed: 25053815]
248. Lee S, Vinegoni C, Sebas M, Weissleder R. Automated motion artifact removal for intravital microscopy, without a priori information. Sci Rep. 2014; 4:4507. [PubMed: 24676021]
249. Vinegoni C, Lee S, Gorbatov R, Weissleder R. Motion compensation using a suctioning stabilizer for intravital microscopy. Intravital. 2012; 1:115–121. [PubMed: 24086796]
250. Lindsay RS, et al. Antigen recognition in the islets changes with progression of autoimmune islet infiltration. J Immunol. 2015; 194:522–530. [PubMed: 25505281]
251. Looney MR, et al. Stabilized imaging of immune surveillance in the mouse lung. Nat Methods. 2011; 8:91–96. [PubMed: 21151136]
252. Headley MB, et al. Visualization of immediate immune responses to pioneer metastatic cells in the lung. Nature. 2016; 531:513–517. [PubMed: 26982733]
253. Dzhagalov IL, Melichar HJ, Ross JO, Herzmark P, Robey EA. Two-photon imaging of the immune system. Curr Protoc Cytom. 2012; Chapter 12(Unit12.26)
254. Li W, et al. Intravital 2-photon imaging of leukocyte trafficking in beating heart. J Clin Invest. 2012; 122:2499–2508. [PubMed: 22706307]
255. Lee S, et al. Real-time in vivo imaging of the beating mouse heart at microscopic resolution. Nat Commun. 2012; 3:1054. [PubMed: 22968700]
256. Lee S, Vinegoni C, Feruglio PF, Weissleder R. Improved intravital microscopy via synchronization of respiration and holder stabilization. J Biomed Opt. 2012; 17:96018–96011. [PubMed: 23085919]
257. Pinkard H, Corbin K, Krummel MF. Spatiotemporal Rank Filtering Improves Image Quality Compared to Frame Averaging in 2-Photon Laser Scanning Microscopy. PLoS One. 2016; 11:e0150430. [PubMed: 26938064]

258. Muriello PA, Dunn KW. Improving Signal Levels in Intravital Multiphoton Microscopy using an Objective Correction Collar. Opt Commun. 2008; 281:1806–1812. [PubMed: 19343075]
259. Yu H, et al. Recent advances in wavefront shaping techniques for biomedical applications. Curr Appl Phys. 2015; 15:632–641.
260. Wang K, et al. Direct wavefront sensing for high-resolution in vivo imaging in scattering tissue. Nat Commun. 2015; 6:7276. [PubMed: 26073070]
261. Shimozawa T, et al. Improving spinning disk confocal microscopy by preventing pinhole cross-talk for intravital imaging. Proc Natl Acad Sci U S A. 2013; 110:3399–3404. [PubMed: 23401517]
262. Vinegoni C, et al. Real-time high dynamic range laser scanning microscopy. Nat Commun. 2016; 7:11077. [PubMed: 27032979]
263. Verveer PJ, et al. High-resolution three-dimensional imaging of large specimens with light sheet-based microscopy. Nat Methods. 2007; 4:311–313. [PubMed: 17339847]
264. Chen BC, et al. Lattice light-sheet microscopy: imaging molecules to embryos at high spatiotemporal resolution. Science. 2014; 346:1257998. [PubMed: 25342811]
265. Soulet D, Paré A, Coste J, Lacroix S. Automated filtering of intrinsic movement artifacts during two-photon intravital microscopy. PLoS One. 2013; 8:e53942. [PubMed: 23326545]
266. Dunn KW, Lorenz KS, Salama P, Delp EJ. IMART software for correction of motion artifacts in images collected in intravital microscopy. Intravital. 2014; 3:e28210. [PubMed: 26090271]
267. Bradley RS, Thorniley MS. A review of attenuation correction techniques for tissue fluorescence. J R Soc Interface. 2006; 3:1–13. [PubMed: 16849213]
268. Schneider CA, Rasband WS, Eliceiri KW. NIH Image to ImageJ: 25 years of image analysis. Nat Methods. 2012; 9:671–675. [PubMed: 22930834]
269. Carpenter AE, et al. CellProfiler: image analysis software for identifying and quantifying cell phenotypes. Genome Biol. 2006; 7:R100. [PubMed: 17076895]
270. Santella A, Du Z, Nowotschin S, Hadjantonakis AK, Bao Z. A hybrid blob-slice model for accurate and efficient detection of fluorescence labeled nuclei in 3D. BMC Bioinformatics. 2010; 11:580. [PubMed: 21114815]
271. Du Z, Santella A, He F, Tiongson M, Bao Z. De novo inference of systems-level mechanistic models of development from live-imaging-based phenotype analysis. Cell. 2014; 156:359–372. [PubMed: 24439388]
272. Miller MA, et al. Targeting autocrine HB-EGF signaling with specific ADAM12 inhibition using recombinant ADAM12 prodomain. Sci Rep. 2015; 5:15150. [PubMed: 26477568]
273. Giedt RJ, Koch PD, Weissleder R. Single cell analysis of drug distribution by intravital imaging. PLoS One. 2013; 8:e60988. [PubMed: 23593370]
274. Peng H, Bria A, Zhou Z, Iannello G, Long F. Extensible visualization and analysis for multidimensional images using Vaa3D. Nat Protoc. 2014; 9:193–208. [PubMed: 24385149]
275. Ortiz D, Briceño JC, Cabrales P. Microhemodynamic parameters quantification from intravital microscopy videos. Physiol Meas. 2014; 35:351–367. [PubMed: 24480871]
276. Ferrell N, et al. Shear stress is normalized in glomerular capillaries following 5/6 nephrectomy. Am J Physiol Renal Physiol. 2015; 308:F588–93. [PubMed: 25587117]
277. Fraser GM, Goldman D, Ellis CG. Comparison of generated parallel capillary arrays to three-dimensional reconstructed capillary networks in modeling oxygen transport in discrete microvascular volumes. Microcirculation. 2013; 20:748–763. [PubMed: 23841679]
278. Frieboes HB, et al. An integrated computational/experimental model of lymphoma growth. PLoS Comput Biol. 2013; 9:e1003008. [PubMed: 23555235]
279. Tovar-Lopez FJ, et al. Structural and hydrodynamic simulation of an acute stenosis-dependent thrombosis model in mice. J Biomech. 2011; 44:1031–1039. [PubMed: 21392770]
280. Thurber GM, Reiner T, Yang KS, Kohler RH, Weissleder R. Effect of Small-Molecule Modification on Single-Cell Pharmacokinetics of PARP Inhibitors. Mol Cancer Ther. 2014; 13:986–995. [PubMed: 24552776]

281. Ritsma L, Vrisekoop N, van Rheenen J. In vivo imaging and histochemistry are combined in the cryosection labelling and intravital microscopy technique. Nat Commun. 2013; 4:2366. [PubMed: 23978961]

282. Zrazhevskiy P, Gao X. Quantum dot imaging platform for single-cell molecular profiling. Nat Commun. 2013; 4:1619. [PubMed: 23511483]

283. Lin JR, Fallahi-Sichani M, Sorger PK. Highly multiplexed imaging of single cells using a high-throughput cyclic immunofluorescence method. Nat Commun. 2015; 6:8390. [PubMed: 26399630]

284. Angelo M, et al. Multiplexed ion beam imaging of human breast tumors. Nat Med. 2014; 20:436–442. [PubMed: 24584119]

285. Lee JH, et al. Fluorescent in situ sequencing (FISSEQ) of RNA for gene expression profiling in intact cells and tissues. Nat Protoc. 2015; 10:442–458. [PubMed: 25675209]

286. Katira P, Bonnecaze RT, Zaman MH. Modeling the mechanics of cancer: effect of changes in cellular and extra-cellular mechanical properties. Front Oncol. 2013; 3:145. [PubMed: 23781492]

287. Gierut JJ, et al. Network-level effects of kinase inhibitors modulate TNF-α-induced apoptosis in the intestinal epithelium. Sci Signal. 2015; 8:ra129. [PubMed: 26671150]

288. Sachs K, Perez O, Pe’er D, Lauffenburger DA, Nolan GP. Causal protein-signaling networks derived from multiparameter single-cell data. Science. 2005; 308:523–529. [PubMed: 15845847]

289. Miller MA, Feng XJ, Li G, Rabitz HA. Identifying biological network structure, predicting network behavior, and classifying network state with High Dimensional Model Representation (HDMR). PLoS One. 2012; 7:e37664. [PubMed: 22723838]

290. Tuncbag N, et al. Network-Based Interpretation of Diverse High-Throughput Datasets through the Omics Integrator Software Package. PLoS Comput Biol. 2016; 12:e1004879. [PubMed: 27096930]

291. Bordbar A, Monk JM, King ZA, Palsson BO. Constraint-based models predict metabolic and associated cellular functions. Nat Rev Genet. 2014; 15:107–120. [PubMed: 24430943]

292. Bordbar A, et al. Personalized whole-cell kinetic models of metabolism for discovery in genomics and pharmacodynamics. Cell Systems. 2015; 1:283–292. [PubMed: 27136057]

293. Iyengar R, Zhao S, Chung SW, Mager DE, Gallo JM. Merging systems biology with pharmacodynamics. Sci Transl Med. 2012; 4:126ps7.

294. Purvis JE, Lahav G. Encoding and decoding cellular information through signaling dynamics. Cell. 2013; 152:945–956. [PubMed: 23452846]

295. Yu JS, Bagheri N. Multi-class and multi-scale models of complex biological phenomena. Curr Opin Biotechnol. 2016; 39:167–173. [PubMed: 27115496]

296. Miller M, et al. Modular design of artificial tissue homeostasis: robust control through synthetic cellular heterogeneity. PLoS Comput Biol. 2012; 8:e1002579. [PubMed: 22829755]

297. Textor J, et al. Random migration and signal integration promote rapid and robust T cell recruitment. PLoS Comput Biol. 2014; 10:e1003752. [PubMed: 25102014]

298. Loudet A, Burgess K. BODIPY dyes and their derivatives: syntheses and spectroscopic properties. Chem Rev. 2007; 107:4891–4932. [PubMed: 17924696]

299. Guo Z, Park S, Yoon J, Shin I. Recent progress in the development of near-infrared fluorescent probes for bioimaging applications. Chem Soc Rev. 2014; 43:16–29. [PubMed: 24052190]

300. Berlier JE, et al. Quantitative comparison of long-wavelength Alexa Fluor dyes to Cy dyes: fluorescence of the dyes and their bioconjugates. J Histochem Cytochem. 2003; 51:1699–1712. [PubMed: 14623938]

301. Ulrich G, Ziessel R, Harriman A. The chemistry of fluorescent bodipy dyes: versatility unsurpassed. Angew Chem Int Ed Engl. 2008; 47:1184–1201. [PubMed: 18092309]

302. Hama Y, et al. A comparison of the emission efficiency of four common green fluorescence dyes after internalization into cancer cells. Bioconjug Chem. 2006; 17:1426–1431. [PubMed: 17105220]

303. Hinkeldey B, Schmitt A, Jung G. Comparative photostability studies of BODIPY and fluorescein dyes by using fluorescence correlation spectroscopy. Chemphyschem. 2008; 9:2019–2027. [PubMed: 18816535]

304. Karolin J, Johansson LBA, Strandberg L, Ny T. Fluorescence and absorption spectroscopic properties of dipyrrometheneboron difluoride (BODIPY) derivatives in liquids, lipid membranes, and proteins. J Am Chem Soc. 1994; 116:7801–7806.

305. Courtis AM, et al. Monoalkoxy BODIPYs--a fluorophore class for bioimaging. Bioconjug Chem. 2014; 25:1043–1051. [PubMed: 24797834]

306. Feazell RP, Nakayama-Ratchford N, Dai H, Lippard SJ. Soluble single-walled carbon nanotubes as longboat delivery systems for platinum(IV) anticancer drug design. J Am Chem Soc. 2007; 129:8438–8439. [PubMed: 17569542]

307. Kosuge H, et al. Near infrared imaging and photothermal ablation of vascular inflammation using single-walled carbon nanotubes. J Am Heart Assoc. 2012; 1:e002568. [PubMed: 23316318]

308. Texier I, et al. Cyanine-loaded lipid nanoparticles for improved in vivo fluorescence imaging. J Biomed Opt. 2009; 14:054005. [PubMed: 19895107]

309. Kamaly N, et al. Development and in vivo efficacy of targeted polymeric inflammation-resolving nanoparticles. Proc Natl Acad Sci U S A. 2013; 110:6506–6511. [PubMed: 23533277]

310. Cassette E, et al. Design of new quantum dot materials for deep tissue infrared imaging. Adv Drug Deliv Rev. 2013; 65:719–731. [PubMed: 22981756]

311. Wegner KD, Hildebrandt N. Quantum dots: bright and versatile in vitro and in vivo fluorescence imaging biosensors. Chem Soc Rev. 2015; 44:4792–4834. [PubMed: 25777768]

312. Wang LW, Peng CW, Chen C, Li Y. Quantum dots-based tissue and in vivo imaging in breast cancer researches: current status and future perspectives. Breast Cancer Res Treat. 2015; 151:7–17. [PubMed: 25833213]

313. Vu TQ, Lam WY, Hatch EW, Lidke DS. Quantum dots for quantitative imaging: from single molecules to tissue. Cell Tissue Res. 2015; 360:71–86. [PubMed: 25620410]

314. Bilan R, Fleury F, Nabiev I, Sukhanova A. Quantum dot surface chemistry and functionalization for cell targeting and imaging. Bioconjug Chem. 2015; 26:609–624. [PubMed: 25710410]

315. Yuan Y, et al. Oligomeric nanoparticles functionalized with NIR-emitting CdTe/CdS QDs and folate for tumor-targeted imaging. Biomaterials. 2014; 35:7881–7886. [PubMed: 24952975]

316. Han HS, et al. Quantum dot/antibody conjugates for in vivo cytometric imaging in mice. Proc Natl Acad Sci U S A. 2015; 112:1350–1355. [PubMed: 25605916]

317. Lin G, Wang X, Yin F, Yong KT. Passive tumor targeting and imaging by using mercaptosuccinic acid-coated near-infrared quantum dots. Int J Nanomedicine. 2015; 10:335–345. [PubMed: 25609948]

318. Liu J, et al. Assessing clinical prospects of silicon quantum dots: studies in mice and monkeys. ACS Nano. 2013; 7:7303–7310. [PubMed: 23841561]

319. Ye L, et al. A pilot study in non-human primates shows no adverse response to intravenous injection of quantum dots. Nat Nanotechnol. 2012; 7:453–458. [PubMed: 22609691]

320. Bakalova R, et al. Delivery of size-controlled long-circulating polymersomes in solid tumours, visualized by quantum dots and optical imaging in vivo. Biotechnol Biotechnol Equip. 2015; 29:175–180. [PubMed: 26019630]

321. Fan Y, et al. Extremely high brightness from polymer-encapsulated quantum dots for two-photon cellular and deep-tissue imaging. Sci Rep. 2015; 5:9908. [PubMed: 25909393]

322. Liu X, Yan CH, Capobianco JA. Photon upconversion nanomaterials. Chem Soc Rev. 2015; 44:1299–1301. [PubMed: 25716767]

323. Park YI, Lee KT, Suh YD, Hyeon T. Upconverting nanoparticles: a versatile platform for wide-field two-photon microscopy and multi-modal in vivo imaging. Chem Soc Rev. 2015; 44:1302–1317. [PubMed: 25042637]

324. Chan YH, et al. Development of ultrabright semiconducting polymer dots for ratiometric pH sensing. Anal Chem. 2011; 83:1448–1455. [PubMed: 21244093]

325. Chen CP, et al. Near-infrared fluorescent semiconducting polymer dots with high brightness and pronounced effect of positioning alkyl chains on the comonomers. ACS Appl Mater Interfaces. 2014; 6:21585–21595. [PubMed: 25394668]

326. Jin Y, Ye F, Zeigler M, Wu C, Chiu DT. Near-infrared fluorescent dye-doped semiconducting polymer dots. ACS Nano. 2011; 5:1468–1475. [PubMed: 21280613]

327. Pu K, Chattopadhyay N, Rao J. Recent advances of semiconducting polymer nanoparticles in In vivo molecular imaging. J Control Release. 2016 In press.

328. Pu K, et al. Semiconducting polymer nanoparticles as photoacoustic molecular imaging probes in living mice. Nat Nanotechnol. 2014; 9:233–239. [PubMed: 24463363]

329. Ge J, et al. Red-Emissive Carbon Dots for Fluorescent, Photoacoustic, and Thermal Theranostics in Living Mice. Adv Mater. 2015; 27:4169–4177. [PubMed: 26045099]

330. Xiong L, Shuhendler AJ, Rao J. Self-luminescing BRET-FRET near-infrared dots for in vivo lymph-node mapping and tumour imaging. Nat Commun. 2012; 3:1193. [PubMed: 23149738]

331. Xu H, et al. Polymer encapsulated upconversion nanoparticle/iron oxide nanocomposites for multimodal imaging and magnetic targeted drug delivery. Biomaterials. 2011; 32:9364–9373. [PubMed: 21880364]

332. Yan B, Boyer JC, Branda NR, Zhao Y. Near-infrared light-triggered dissociation of block copolymer micelles using upconverting nanoparticles. J Am Chem Soc. 2011; 133:19714–19717. [PubMed: 22082025]

333. Viger ML, Grossman M, Fomina N, Almutairi A. Low power upconverted near-IR light for efficient polymeric nanoparticle degradation and cargo release. Adv Mater. 2013; 25:3733–3738. [PubMed: 23722298]

334. Wu S, Butt HJ. Near-Infrared-Sensitive Materials Based on Upconverting Nanoparticles. Adv Mater. 2015; 28:1208–1226. [PubMed: 26389516]

335. Hong Y, Lam JW, Tang BZ. Aggregation-induced emission: phenomenon, mechanism and applications. Chem Commun (Camb). 2009:4332–4353. [PubMed: 19597589]

336. Lager E, Liu J, Aguilar-Aguilar A, Tang BZ, Peña-Cabrera E. Novel meso-polyarylamine-BODIPY hybrids: synthesis and study of their optical properties. J Org Chem. 2009; 74:2053–2058. [PubMed: 19203181]

337. Zhang X, et al. Aggregation induced emission-based fluorescent nanoparticles: fabrication methodologies and biomedical applications. J Mater Chem B. 2014; 2:4398–4414.

338. Zhang X, et al. Aggregation-induced emission dye based luminescent silica nanoparticles: facile preparation, biocompatibility evaluation and cell imaging applications. RSC Advances. 2014; 4:10060–10066.

339. Zhang X, et al. Polymerizable aggregation-induced emission dye-based fluorescent nanoparticles for cell imaging applications. Polym Chem. 2014; 5:356–360.

340. Liu M, et al. Polylysine crosslinked AIE dye based fluorescent organic nanoparticles for biological imaging applications. Macromol Biosci. 2014; 14:1260–1267. [PubMed: 24854875]

341. Liu M, et al. Ultrabright and biocompatible AIE dye based zwitterionic polymeric nanoparticles for biological imaging. RSC Advances. 2014; 4:35137–35143.

342. Zhang X, Yang B, Zhang Y, Wei Y. Facile preparation of water dispersible red fluorescent organic nanoparticles and their cell imaging applications. Tetrahedron. 2014; 70:3553–3559.

343. Wang K, Zhang X, Zhang X, Yang B, Li… Z. Fabrication of cross-linked fluorescent polymer nanoparticles and their cell imaging applications. J Mater Chem C Mater Opt Electron Devices. 2015; 3:1854–1860.

344. Ding D, et al. Ultrabright organic dots with aggregation-induced emission characteristics for real-time two-photon intravital vasculature imaging. Adv Mater. 2013; 25:6083–6088. [PubMed: 24038281]

345. Zhu A, Qu Q, Shao X, Kong B, Tian Y. Carbon-dot-based dual-emission nanohybrid produces a ratiometric fluorescent sensor for in vivo imaging of cellular copper ions. Angew Chem Int Ed Engl. 2012; 51:7185–7189. [PubMed: 22407813]

346. Liu H, et al. Intracellular Temperature Sensing: An Ultra-bright Luminescent Nanothermometer with Non-sensitivity to pH and Ionic Strength. Sci Rep. 2015; 5:14879. [PubMed: 26445905]

347. Gao W, Chan JM, Farokhzad OC. pH-Responsive nanoparticles for drug delivery. Mol Pharm. 2010; 7:1913–1920. [PubMed: 20836539]

348. Mura S, Nicolas J, Couvreur P. Stimuli-responsive nanocarriers for drug delivery. Nat Mater. 2013; 12:991–1003. [PubMed: 24150417]

349. Liu J, et al. pH-sensitive nano-systems for drug delivery in cancer therapy. Biotechnol Adv. 2014; 32:693–710. [PubMed: 24309541]

350. Kanamala M, Wilson WR, Yang M, Palmer BD, Wu Z. Mechanisms and biomaterials in pH-responsive tumour targeted drug delivery: A review. Biomaterials. 2016; 85:152–167. [PubMed: 26871891]

351. Amali AJ, Awwad NH, Rana RK, Patra D. Nanoparticle assembled microcapsules for application as pH and ammonia sensor. Anal Chim Acta. 2011; 708:75–83. [PubMed: 22093347]

352. Gao F, et al. Core-shell fluorescent silica nanoparticles for sensing near-neutral pH values. Microchimica Acta. 2011; 172:327–333.

353. Ray A, Koo Lee YE, Epstein T, Kim G, Kopelman R. Two-photon nano-PEBBLE sensors: subcellular pH measurements. Analyst. 2011; 136:3616–3622. [PubMed: 21773602]

354. Ray A, Lee YE, Kim G, Kopelman R. Two-photon fluorescence imaging super-enhanced by multishell nanophotonic particles, with application to subcellular pH. Small. 2012; 8:2213–2221. [PubMed: 22517569]

355. Somers RC, et al. A Nanocrystal-based Ratiometric pH Sensor for Natural pH Ranges. Chem Sci. 2012; 3:2980–2985. [PubMed: 26413260]

356. Strobl M, Rappitsch T, Borisov SM, Mayr T, Klimant I. NIR-emitting aza-BODIPY dyes–new building blocks for broad-range optical pH sensors. Analyst. 2015; 140:7150–7153. [PubMed: 26402484]

357. Han F, Xu Y, Jiang D, Qin Y, Chen H. A BODIPY-derived fluorescent probe for cellular pH measurements. Anal Biochem. 2013; 15:106–113.

358. Rink TJ, Tsien RY, Pozzan T. Cytoplasmic pH and free Mg2+ in lymphocytes. J Cell Biol. 1982; 95:189–196. [PubMed: 6815204]

359. Koo YE, et al. Real-time measurements of dissolved oxygen inside live cells by organically modified silicate fluorescent nanosensors. Anal Chem. 2004; 76:2498–2505. [PubMed: 15117189]

360. Xu H, Aylott JW, Kopelman R, Miller TJ, Philbert MA. A real-time ratiometric method for the determination of molecular oxygen inside living cells using sol-gel-based spherical optical nanosensors with applications to rat C6 glioma. Anal Chem. 2001; 73:4124–4133. [PubMed: 11569801]

361. Thambi T, et al. Hypoxia-responsive polymeric nanoparticles for tumor-targeted drug delivery. Biomaterials. 2014; 35:1735–1743. [PubMed: 24290696]

362. Kiyose K, et al. Hypoxia-sensitive fluorescent probes for in vivo real-time fluorescence imaging of acute ischemia. J Am Chem Soc. 2010; 132:15846–15848. [PubMed: 20979363]

363. Cui L, et al. A new prodrug-derived ratiometric fluorescent probe for hypoxia: high selectivity of nitroreductase and imaging in tumor cell. Org Lett. 2011; 13:928–931. [PubMed: 21268631]

364. Okuda K, et al. 2-Nitroimidazole-tricarbocyanine conjugate as a near-infrared fluorescent probe for in vivo imaging of tumor hypoxia. Bioconjug Chem. 2012; 23:324–329. [PubMed: 22335430]

365. Korzeniowska B, Raspe M, Wencel D, Woolley… R. Development of organically modified silica nanoparticles for monitoring the intracellular level of oxygen using a frequency-domain FLIM platform. RSC Advances. 2015; 5:36938–36947.

366. Zhao Q, et al. Fluorescent/phosphorescent dual-emissive conjugated polymer dots for hypoxia bioimaging. Chem Sci. 2015; 6:1825–1831. [PubMed: 28694947]

367. Lee YE, et al. Near infrared luminescent oxygen nanosensors with nanoparticle matrix tailored sensitivity. Anal Chem. 2010; 82:8446–8455. [PubMed: 20849084]

368. Liu H, et al. Development of polymeric nanoprobes with improved lifetime dynamic range and stability for intracellular oxygen sensing. Small. 2013; 9:2639–2648. [PubMed: 23519925]

369. Wu C, Bull B, Christensen K, McNeill J. Ratiometric single-nanoparticle oxygen sensors for biological imaging. Angew Chem Int Ed Engl. 2009; 48:2741–2745. [PubMed: 19253320]

370. Wang XD, et al. Ultra-small, highly stable, and sensitive dual nanosensors for imaging intracellular oxygen and pH in cytosol. J Am Chem Soc. 2012; 134:17011–17014. [PubMed: 23017056]

371. Liu J, et al. Ultrasensitive nanosensors based on upconversion nanoparticles for selective hypoxia imaging in vivo upon near-infrared excitation. J Am Chem Soc. 2014; 136:9701–9709. [PubMed: 24956326]

372. Zheng X, et al. Hypoxia-specific ultrasensitive detection of tumours and cancer cells in vivo. Nat Commun. 2015; 6:5834. [PubMed: 25556360]

373. Zheng X, et al. Tracking Cancer Metastasis In Vivo by Using an Iridium-Based Hypoxia-Activated Optical Oxygen Nanosensor. Angew Chem Int Ed Engl. 2015; 54:8094–8099. [PubMed: 26037656]

374. Zhang G, Palmer GM, Dewhirst MW, Fraser CL. A dual-emissive-materials design concept enables tumour hypoxia imaging. Nat Mater. 2009; 8:747–751. [PubMed: 19668206]

375. van Rijt SH, et al. Protease-mediated release of chemotherapeutics from mesoporous silica nanoparticles to ex vivo human and mouse lung tumors. ACS Nano. 2015; 9:2377–2389. [PubMed: 25703655]

376. von Maltzahn G, et al. Nanoparticle self-assembly gated by logical proteolytic triggers. J Am Chem Soc. 2007; 129:6064–6065. [PubMed: 17447766]

377. Hu J, Zhang G, Liu S. Enzyme-responsive polymeric assemblies, nanoparticles and hydrogels. Chem Soc Rev. 2012; 41:5933–5949. [PubMed: 22695880]

378. de la Rica R, Aili D, Stevens MM. Enzyme-responsive nanoparticles for drug release and diagnostics. Adv Drug Deliv Rev. 2012; 64:967–978. [PubMed: 22266127]

379. Vandooren J, Opdenakker G, Loadman PM, Edwards DR. Proteases in cancer drug delivery. Adv Drug Deliv Rev. 2016; 97:144–155. [PubMed: 26756735]

380. Weissleder R, Tung CH, Mahmood U, Bogdanov A. In vivo imaging of tumors with protease-activated near-infrared fluorescent probes. Nat Biotechnol. 1999; 17:375–378. [PubMed: 10207887]

381. Mahmood U, Weissleder R. Near-infrared optical imaging of proteases in cancer. Mol Cancer Ther. 2003; 2:489–496. [PubMed: 12748311]

382. Wang J, Zhang L, Chen M, Gao S, Zhu L. Activatable Ferritin Nanocomplex for Real-Time Monitoring of Caspase-3 Activation during Photodynamic Therapy. ACS Appl Mater Interfaces. 2015; 7:23248–23256. [PubMed: 26388178]

383. Gounaris E, et al. Live imaging of cysteine-cathepsin activity reveals dynamics of focal inflammation, angiogenesis, and polyp growth. PLoS One. 2008; 3:e2916. [PubMed: 18698347]

384. Miller MA, et al. Proteolytic Activity Matrix Analysis (PrAMA) for simultaneous determination of multiple protease activities. Integr Biol (Camb). 2011; 3:422–438. [PubMed: 21180771]

385. Planck SR, et al. Impact of IL-1 signalling on experimental uveitis and arthritis. Ann Rheum Dis. 2012; 71:753–760. [PubMed: 22267332]

386. Kastrup CJ, et al. Painting blood vessels and atherosclerotic plaques with an adhesive drug depot. Proc Natl Acad Sci U S A. 2012; 109:21444–21449. [PubMed: 23236189]

387. Forssen EA, et al. Fluorescence imaging studies for the disposition of daunorubicin liposomes (DaunoXome) within tumor tissue. Cancer Res. 1996; 56:2066–2075. [PubMed: 8616852]

388. Bell DH. Characterization of the fluorescence of the antitumor agent, mitoxantrone. Biochim Biophys Acta. 1988; 949:132–137. [PubMed: 3334848]

389. Pautke C, et al. Characterization of eight different tetracyclines: advances in fluorescence bone labeling. J Anat. 2010; 217:76–82. [PubMed: 20456523]

390. Nakasone ES, et al. Imaging tumor-stroma interactions during chemotherapy reveals contributions of the microenvironment to resistance. Cancer Cell. 2012; 21:488–503. [PubMed: 22516258]

391. Bhuniya S, et al. A fluorescence off-on reporter for real time monitoring of gemcitabine delivery to the cancer cells. Chem Commun (Camb). 2013; 49:7141–7143. [PubMed: 23831834]

392. Lazo JS, et al. Chemical synthesis and biological activity of a novel fluorescent etoposide derivative. Biochem Pharmacol. 1997; 53:715–722. [PubMed: 9113091]

393. Jagodinsky JC, et al. Evaluation of fluorophore-tethered platinum complexes to monitor the fate of cisplatin analogs. J Biol Inorg Chem. 2015; 20:1081–1095. [PubMed: 26323351]

394. Kim E, Yang KS, Weissleder R. Bioorthogonal small molecule imaging agents allow single-cell imaging of MET. PLoS One. 2013; 8:e81275. [PubMed: 24265843]

395. Crivellato E, et al. The fluorescent probe Bodipy-FL-verapamil is a substrate for both P-glycoprotein and multidrug resistance-related protein (MRP)-1. J Histochem Cytochem. 2002; 50:731–734. [PubMed: 11967284]

396. Rosati A, et al. Bodipy-FL-verapamil: a fluorescent probe for the study of multidrug resistance proteins. Cell Oncol. 2004; 26:3–11. [PubMed: 15371652]

397. Sprachman MM, Laughney AM, Kohler RH, Weissleder R. In Vivo Imaging of Multidrug Resistance Using a Third Generation MDR1 Inhibitor. Bioconjug Chem. 2014; 25:1137–1142. [PubMed: 24806886]

398. Maiti S, et al. Gemcitabine-coumarin-biotin conjugates: a target specific theranostic anticancer prodrug. J Am Chem Soc. 2013; 135:4567–4572. [PubMed: 23461361]

399. Lin W, Chen T. A vinblastine fluorescent probe for pregnane X receptor in a time-resolved fluorescence resonance energy transfer assay. Anal Biochem. 2013; 443:252–260. [PubMed: 24044991]

400. Lukinavičius G, et al. Fluorogenic probes for live-cell imaging of the cytoskeleton. Nat Methods. 2014; 11:731–733. [PubMed: 24859753]

401. Zheng YR, et al. Pt(IV) prodrugs designed to bind non-covalently to human serum albumin for drug delivery. J Am Chem Soc. 2014; 136:8790–8798. [PubMed: 24902769]

402. Carlson JC, Meimetis LG, Hilderbrand SA, Weissleder R. BODIPY-tetrazine derivatives as superbright bioorthogonal turn-on probes. Angew Chem Int Ed Engl. 2013; 52:6917–6920. [PubMed: 23712730]

403. Meimetis LG, Carlson JC, Giedt RJ, Kohler RH, Weissleder R. Ultrafluorogenic coumarin-tetrazine probes for real-time biological imaging. Angew Chem Int Ed Engl. 2014; 53:7531–7534. [PubMed: 24915832]

404. Stephanopoulos N, Francis MB. Choosing an effective protein bioconjugation strategy. Nat Chem Biol. 2011; 7:876–884. [PubMed: 22086289]

405. Dahlman JE, et al. In vivo endothelial siRNA delivery using polymeric nanoparticles with low molecular weight. Nat Nanotechnol. 2014; 9:648–655. [PubMed: 24813696]

406. Liu P, Yu H, Sun Y, Zhu M, Duan Y. A mPEG-PLGA-b-PLL copolymer carrier for adriamycin and siRNA delivery. Biomaterials. 2012; 33:4403–4412. [PubMed: 22436800]

407. Vader P, van der Aa LJ, Engbersen JF, Storm G, Schiffelers RM. A method for quantifying cellular uptake of fluorescently labeled siRNA. J Control Release. 2010; 148:106–109. [PubMed: 20600397]

408. Dunne J, et al. The apparent uptake of fluorescently labeled siRNAs by electroporated cells depends on the fluorochrome. Oligonucleotides. 2003; 13:375–380. [PubMed: 15000828]

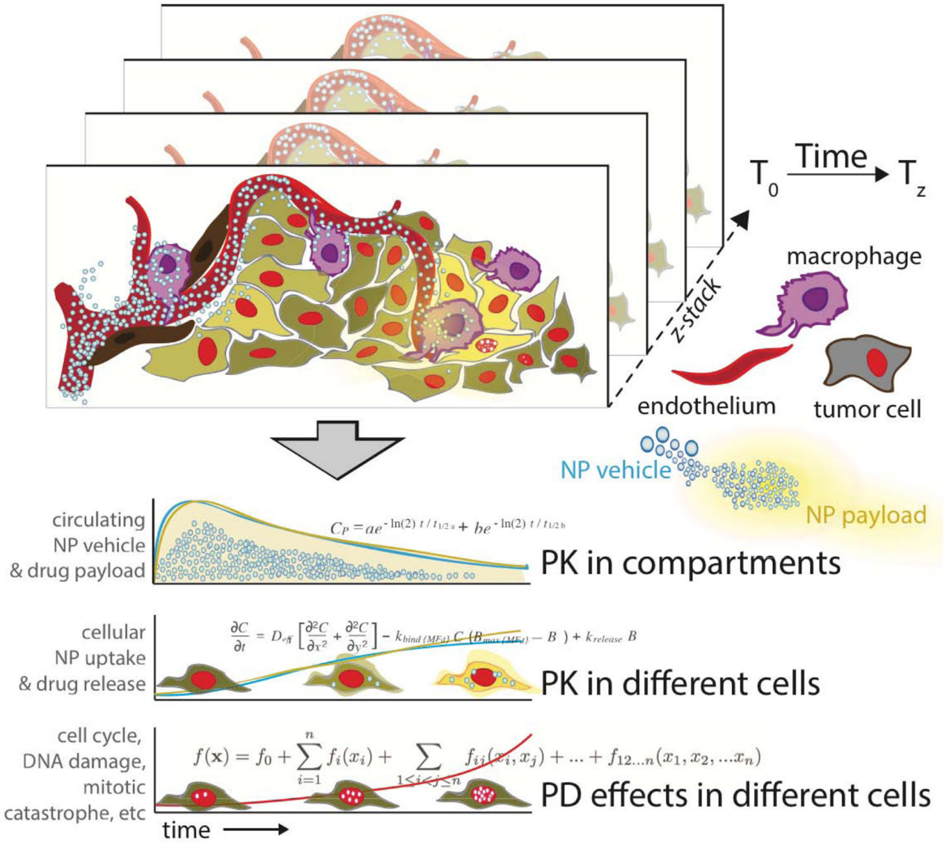

Fig. 1.

From imaging to quantitative pharmacology. The schematic diagram illustrates the different pharmacological compartments (for specific example see Fig. 2). 3D stacks are acquired over time, often over many hours or even days. Image fiducials, rigid registration, motion reduction and anatomic landmarks are all used to co-register image datasets. Information is extracted manually (e.g. ROI measurements) or automatically through image processing software. Data points are tabulated and used to calculate pharmacological parameters at the single cell or population levels.

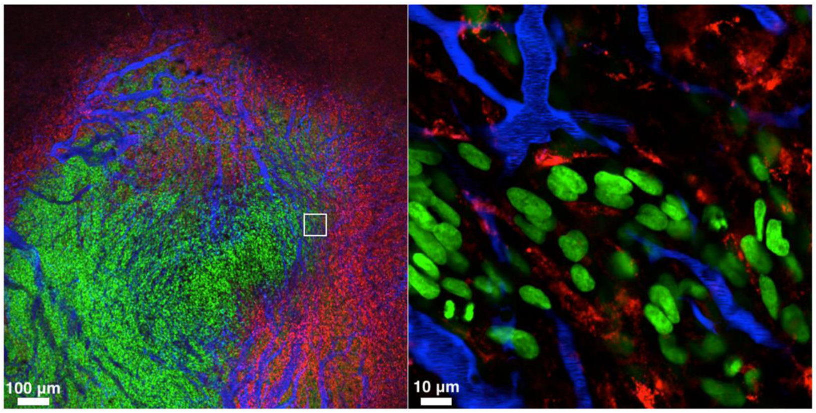

Fig. 2.

Main compartments relevant to NP delivery in tumors. The three compartments are tumor cells (green; HT1080-GFP), tumor associated macrophages (TAM; red; labeled with Ferumoxytol-VT680) and microvasculature (blue; containing Angiosense, a long circulating NP). Timing after administration and type of NP are the primary determinants of NP location (note that the red and blue NP are in different compartments since they were administered 24 hours apart). The other important determinant of delivery is the heterogeneity of the different compartments. All three compartments are heterogenous and often unpredictable unless interrogated by real-time imaging: microvessels often show hyper leaky areas, chaotic flow, non-perfusion, stagnant flow and shunting; tumor cells are highly heterogenous, often have different NP uptake properties as well as different distances from microvessels; and phagocytic cells comprise different types of TAM, monocytes, neutrophils and dendritic cells, all with different properties and functions. The white box in the left image represents the area of higher magnification on the right.

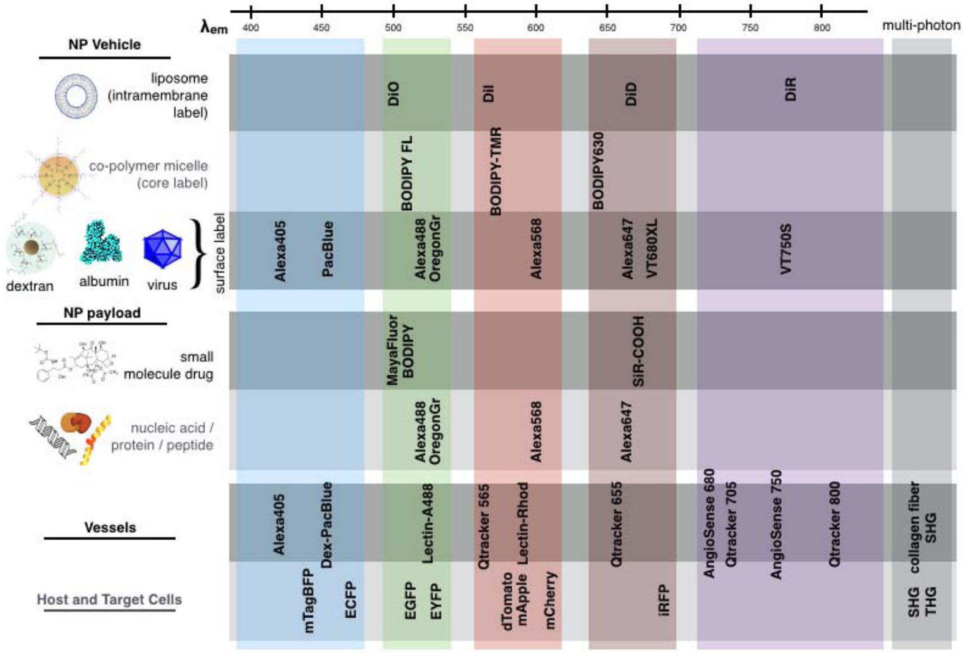

Figure 3.

Strategy of fluorescent labeling for multichannel IVM imaging. Most modern confocal and multiphoton imaging systems allow analysis of NP vehicle, payload, and physiological features (e.g., vascular, stromal and immune cell populations) using 4–6 fluorescent channels. Specialized equipment and analysis tools can expand this number. We commonly employ different fluorochromes (see Fig. 4 for specific choices) for IVM; among the generally robust dyes listed above, hydrophobicity is the main determinant of applicability to a particular NP or payload system (rows). Multi-photon excitation can apply to many listed fluorophores, and also enables second- and, less commonly, third-harmonic generation imaging (SHG and THG, respectively) of tissue and cellular structures. In general, 400–450 nm emitting fluorophores are reserved for applications with low signal or resolution requirement due to their relatively poor physicochemical properties and high tissue scattering / autofluorescence.

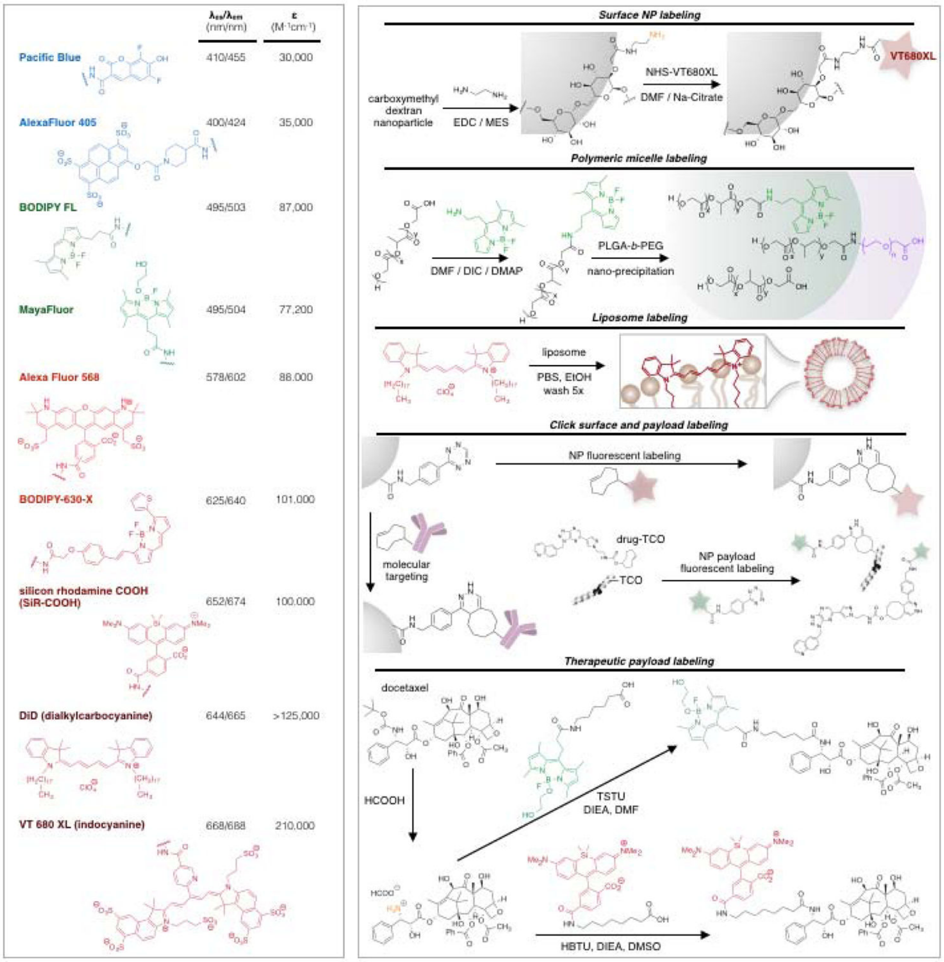

Fig. 4.

Commonly used fluorochromes for IVM and conjugation strategies.

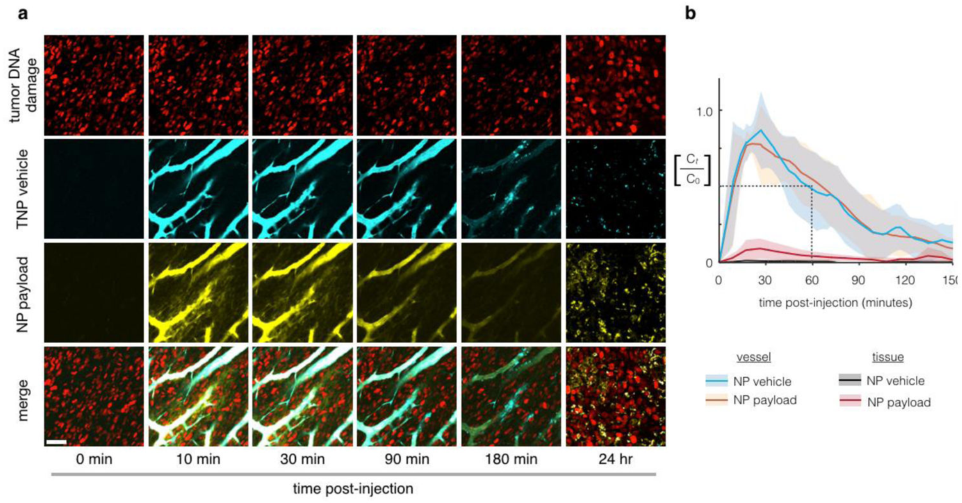

Fig. 5.

Pharmacokinetic analysis of a model nanoparticle shows extended microvasculature half-life and heterogeneous tissue accumulation. Multichannel imaging allows temporal and spatial analysis of both NP and payload distribution. In this example, we monitor the circulation and release of a fluorescent Pt compound from a PEGylated NP [Miller et al., 2015, Nat Commun, 6, 8692]. Nanoparticle concentrations are monitored (a) and quantified (b) using time-lapse confocal fluorescence microscopy in the dorsal window chamber model. Nanoencapsulation extends the initial microvasculature half-life to 55 min, which represents a > 5-fold increase compared to unencapsulated Pt(II) compounds (cisplatin and carboplatin related compounds) in the same animal model [Miller et al., 2014, Chem Med Chem, 9, 1131–5]. Scale bar 50 μm; thick lines and shading denote mean +/− s.e.m. (n=6). Modified from ref. [Miller et al., 2015, Nat Commun, 6, 8692].

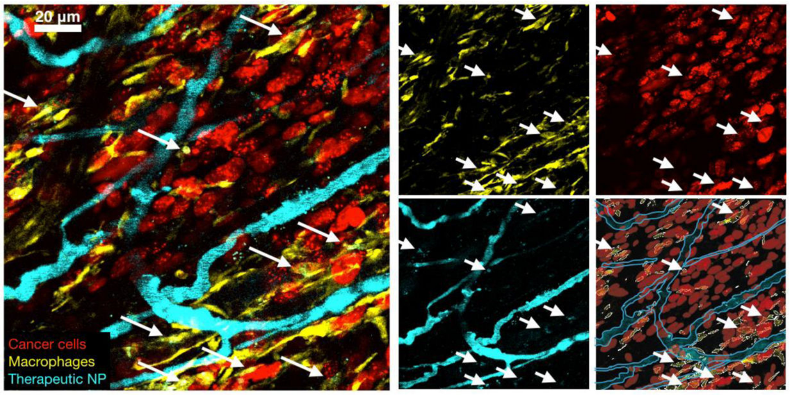

Fig. 6. Multichannel PK/PD imaging of a therapeutic nanoparticle

A PLGA-PEG nanoparticle (cyan in microvessles) is observed as it enters tumor associated macrophages (TAM) ~30 minutes after administration. TAM uptake is highlighted by white arrows. TAM are marked by GFP in a reconstituted mouse model of 53BP1-mApple containing fibrosarcoma cells (HT1080). Red cells with many nuclear puncta are undergoing NP-associated DNA damage.

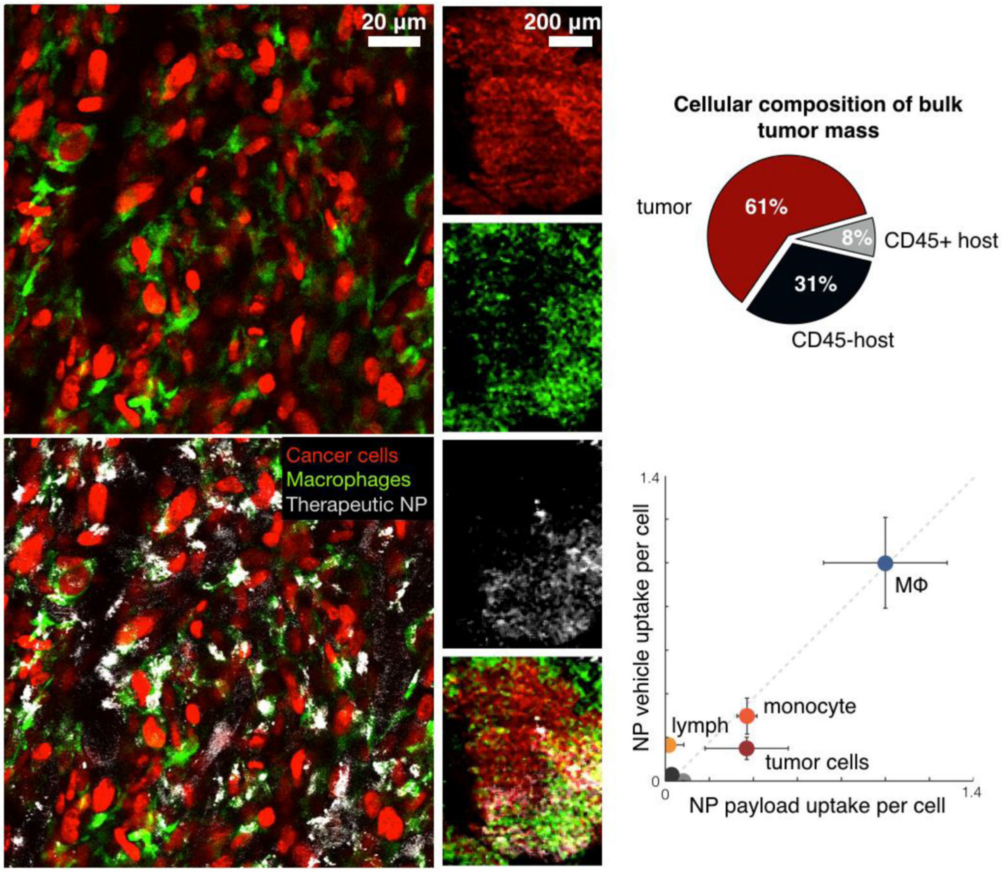

Fig. 7. Different therapeutic NPs including those in clinical use often show prominent uptake in TAM rather than in cancer cells

Nonetheless, therapeutic efficacy is achieved by slow release of payload from TAM to neighboring tumors cells [Miller et al., 2015, Nat Commun, 6, 8692]. The specific examples shown here relate to PLGA-PEG nanoparticles similar to those in clinical trials [Min et al., 2015, Chem Rev, 115, 11147–90]. Note the predominant uptake of NPs in GFP+ TAM (left). Even at lower magnification (middle), NP accumulation mirrors that of TAM distribution. Right: quantitation of TNP uptake (modified from [Miller et al., 2015, Nat Commun, 6, 8692]).

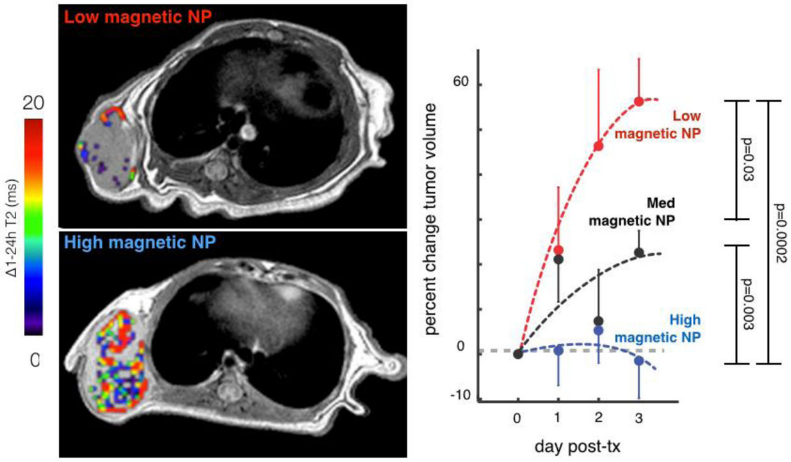

Fig. 8.

MRI of magnetic NPs predicts therapeutic NP efficacy. Left: Example cross-sectional T2 images of tumors accumulating low and high intratumoral magnetic NP, with a pseudo-color overlay to indicate the difference in T2 within the manually segmented tumor region. Right: Pre-therapeutic MRI of magnetic NPs predicts accumulation and response to paclitaxel-loaded NPs. Tumor progression in HT1080 tumors was ranked according to low, medium, and high magnetic NP values as measured by MRI. Error bars denote S.E.M. (total n=33). Modified from ref. [Miller et al., 2015, Sci Transl Med, 7, 314ra183].